ORNL/TM-2021/2113

Development of CTF Modeling of Interfacial Drag, Wall Shear, and Interfacial Heat Transfer for Bubbly and Annular Mist Flow Regimes

V. Kumar
B. Hizoum
R. Salko

July 30, 2021

OAK RIDGE National Laboratory

ORNL IS MANAGED BY UT-BATTELLE LLC FOR THE US DEPARTMENT OF ENERGY

ORNL/TM-2021/2113

Nuclear Energy and Fuel Cycle Division

Development of CTF Modeling of Interfacial Drag, Wall Shear, and Interfacial Heat Transfer for Bubbly and Annular Mist Flow Regimes

Author(s)

V. Kumar B. Hizoum R. Salko

Date Published: July 30, 2021

Prepared by
OAK RIDGE NATIONAL LABORATORY
Oak Ridge, TN 37831-6283
managed by
UT-Battelle LLC
for the
US DEPARTMENT OF ENERGY
under contract DE-AC05-00OR22725

CONTENTS

LIST OF FIGURES

LIST OF TABLES

ABBREVIATIONS

BFBT BWR full-size fine-mesh bundle test

BWR boiling water reactor

CASL Consortium for Advanced Simulation of Light Water Reactors

DREAM Differential Evolution Adaptive Metropolis

FY fiscal year

GE General Electric

GP Gaussian process

HTC heat transfer coefficient

M&S modeling and simulation

MCMC Markov-chain Monte Carlo

ONB onset of nucleate boiling

PDF probability density function

PSBT PWR subchannel and bundle tests

PWR pressurized water reactor

RMSE root mean squared error

T/H thermal hydraulics

ABSTRACT

This milestone report discusses improvements to CTF closure models for modeling of bubbly and annular mist two-phase flow conditions, which are important for accurate modeling and simulation for boiling water reactor (BWR) conditions. Models that were improved include the two-phase wall shear, wall boiling, and phase mass and heat transfer. A new flow regime map was implemented to improve on the prediction of transition to annular flow, which was generally largely over-predicted by the legacy CTF flow regime map. The annular mist interfacial drag models were also reviewed and new models were proposed for implementation into the code. In addition to implementing new models, an activity was performed to calibrate these new models to experimental data using a Markov Chain Monte Carlo technique, thus further improving their accuracy. Finally, new experiments were implemented into the CTF validation matrix which add more two-phase pressure drop and void measurements for the assessment of CTF for modeling of BWRs. The results show that the Chisholm model, which was implemented and then calibrated, results in significantly improved comparison against the Riso two-phase pressure drop data. Furthermore, improvements in the implicit heat transfer and wall boiling models resulted in good agreement with the void measurement data.

1. INTRODUCTION

During the Consortium for Advanced Simulation of Light Water Reactors (CASL) program, the thermal hydraulics (T/H) subchannel code, CTF, was developed for standalone and coupled simulations of pressurized water reactor (PWR) geometry and operating conditions. During this time, some work was done to assess the code for boiling water reactor (BWR) conditions, but very little development work was done to improve on modeling accuracy and features for that type of reactor design. In the time since the completion of CASL, CTF is now being further developed to support modeling of BWRs. This requires adding support for modeling of BWR-specific geometry, improvement of the code solution algorithm for modeling of two-phase flow, and improvement in model accuracy. Work was done on the first two tasks and documented in an earlier milestone report Salko et al. [2021]. This project and associated milestone report is focused on improving the accuracy of the CTF solution for BWR operating conditions. For the sake of completeness, a high-level overview of all planned CTF development activities for fiscal year (FY)s 20 and 21 in support of BWR modeling and simulation (M&S) is presented in Table 1 (originally published in Salko et al. [2021], but updated in this report).

A previous milestone report released last year Salko et al. [2020b] reported progress toward a similar goal to improve CTF closure model accuracy for BWR operating conditions. The previous report focused primarily on the bubbly flow regimes (small bubble and slug, as named in the CTF flow regime map). The previous effort implemented an improved subcooled boiling model and a bubbly flow drift-flux–based interfacial drag model. A brief review of the annular mist flow regime interfacial drag model and the flow regime map was also performed. Additionally, a preliminary calibration of closure model multipliers was performed to demonstrate an approach for calibrating models to improve CTF predictions.

This milestone effort expands on the activities presented in the previous report by performing a deeper analysis of the wall and interfacial heat transfer models, the two-phase pressure drop model, and annular mist interfacial drag models. To improve on the testing of CTF closure models and to provide more data for calibration efforts, the validation matrix was expanded with additional, previously un-modeled tests from the Riso facility and with a set of cases from the FRIGG tests. The FRIGG tests are documented in Section 2.1, and the Riso tests are documented in Section 2.2. The implementation of a quality-based two-phase pressure drop model is presented in Section 3.1. A more thorough review of the wall heat transfer model that was implemented in Kumar and Salko [2020], which led to several improvements to the model form, is discussed in Section 3.2. The review and improvements of the phase heat transfer model are presented in Section 3.3. Because it was found that the legacy CTF flow regime map will often greatly overpredict the transition to annular flow, a new flow regime map was implemented, as discussed in Section 3.4. The implementation of new droplet interfacial drag models for modeling of annular mist flow is presented in Section 3.5. Finally, the expansion of the calibration framework and extension to new closure models is presented in Section 4..

Table 1. Summary of activities required for improvement of CTF modeling of BWRs (reproduced from Salko et al. [2021])

Activity	Status	Documentation
Geometry improvements		
Addition of inlet orifice map	✓	Salko et al. [2020a]
Support for large channel box radii	✓	Salko et al. [2020a]
Addition of support for axially varying water rods	✓	Salko et al. [2020a]
Support for mixed fuel cores	✓	Salko et al. [2021]
Modeling of upper plenum	✓	Salko et al. [2021]
Two-phase form loss model	✠	Salko et al. [2021]
Lower tie-plate form loss model	✓	Salko et al. [2021]
Bypass modeling	✠	Abarca et al. [2021]
Part-length rods	✓	Salko and Kumar [2020]
Quarter symmetry support	✓	Salko et al. [2020a]
Modeling improvements		
Bubbly flow drift flux model	✓	Salko et al. [2020b]
Subcooled boiling model	✓	Salko et al. [2020b]
Closure model calibration demonstration	✓	Salko et al. [2020b]
Drift flux and wall shear calibration	✠	Section 4.
Inclusion of FRIGG data in validation matrix	✓	Section 2.1
Expansion of Riso validation tests	✓	Section 2.2
Assessment of void drift and turbulent mixing	※	Future work
Wall shear model	✓	Section 3.1
Flow regime map	✓	Section 3.4
Annular mist interfacial drag assessment	✠	Section 3.5
Wall heat transfer review	✓	Section 3.2
Improvements to two-phase validation matrix infrastructure	✓	Salko and Kumar [2020]
Addition of boiling validation tests to validation matrix	✓	Salko and Kumar [2020]
Numerical improvements		
Outer iteration loop	✓	Salko et al. [2020a]
Governing equation linearization	✠	Salko et al. [2021]
Timestep review and improvement	✠	Salko et al. [2021]
Parallelization improvements	✓	Salko et al. [2021]
Pressure balance loop performance improvements	✓	Salko et al. [2020a]
Solver improvements	✠	Salko et al. [2020a]

✓= Complete
✠= Work performed, but future work required
※= Task pending, to be completed this fiscal year
Items in italics addressed this milestone

2. VALIDATION MATRIX

2.1 FRIGG DATA

The FRIGG test facility is a test loop that is operated by the Swedish company ASEA ATOM. The facility has been in operation since the 1960s and has been used for testing of many BWR fuel designs over the years. The test results that were obtained and used for this project were the OF-64 tests, which were performed in 1969 Nylund and Eklund [1970]. All of the test results obtained are new additions to the CTF validation matrix. The OF-64 tests consisted of an 8×8 electrically heated rod bundle that was representative of the Oskarshamn-I fuel assembly. Forty experiments were carried out at 48 and 68 bar using a nonuniform axial and radial power distribution and a range of mass fluxes and bundle powers representative of BWR operating conditions. Void measurements were made via a gamma-ray attenuation system at 10 axial locations in the assembly. Measurements were made in five radial zones, allowing for characterization of the radial void distribution. For this initial work, only the bundle-average void was compared against CTF predictions. Note that the new flow regime map discussed in Section 3.4 was utilized for these tests, which includes the correction to the annular mist film interfacial drag discussed in Section 3.5.2.

The entire process of building the CTF models, running cases, comparing results to experimental data, and generating figures was automated by including the tests in the CTF validation matrix. This allows for rapid reassessment of CTF results when any changes are made to the code, and it simplifies updating the CTF Validation Manual Salko et al. [2017b].

The summary of the comparisons of CTF void predictions and experimental measurements is shown in Fig. 1 using the baseline (non-improved) CTF models. As shown in the figure, there is a tendency for CTF to over-predict the void at all void levels; however, there does seem to be a slightly greater over-prediction in the lower void (bubbly flow) regimes. This observation is consistent with what was previously observed for the BWR full-size fine-mesh bundle test (BFBT) tests.

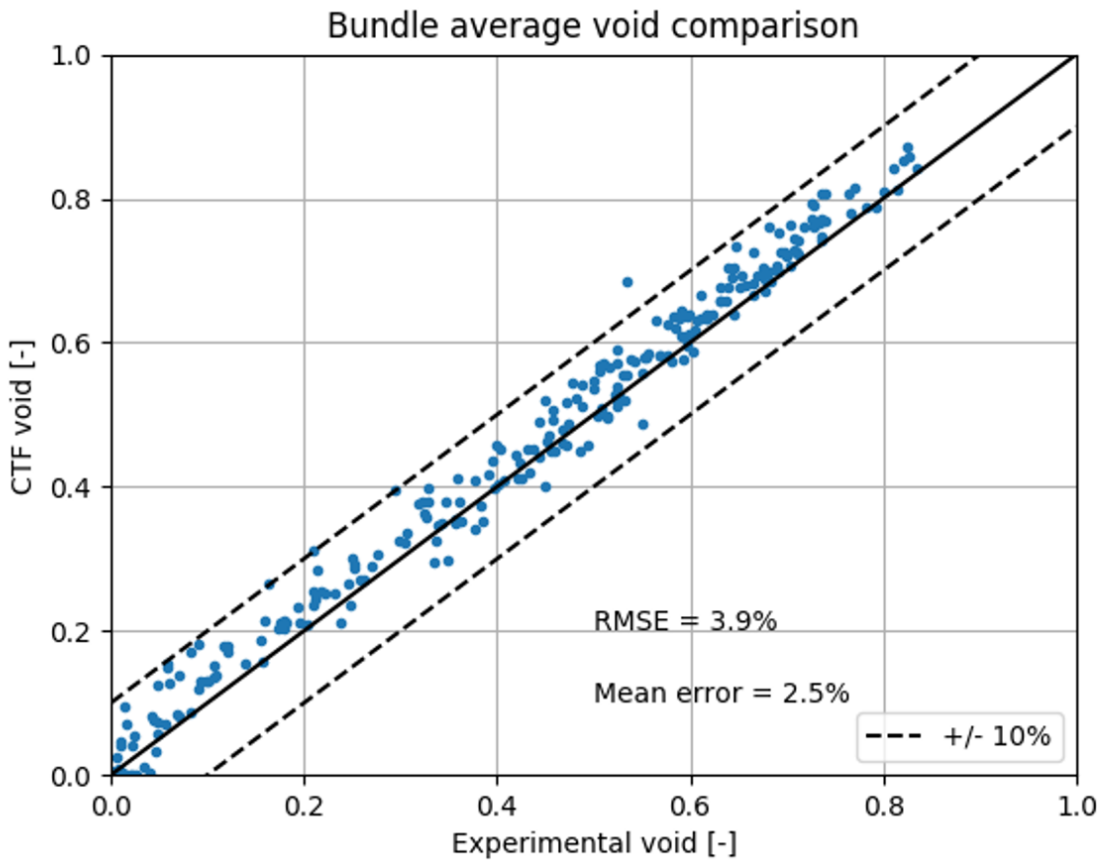

Figure 1. Comparison of CTF-predicted void to FRIGG OF-64 measurements when using the baseline CTF models.

2.2 RISO DATA

The Riso experimental facility included tests of highly voided steam/water mixtures flowing upwards in tubular and annular geometries Wurtz [1978]. More than 250 tests were performed and included both heated and unheated configurations. The flow conditions were set up so that the flows were primarily in the annular mist flow regime. Measurements were made to determine film flow rate, droplet flow rate, film thickness, and two-phase pressure drop. Groups of tests were identified by a series number, which are summarized in Table 2. All of the tubular geometry tests were originally modeled by Wysocki (Wysocki and Salko [2016]). The annular geometry tests were not modeled during this original study, but they are important to include because they are more consistent with subchannel geometry, so both Series 100 and 500 tests were added to the validation matrix as part of this work.

The driver script that builds the CTF input decks for the Riso facility was expanded to support the annular geometry required for modeling the 100- and 500-series tests. The CTF models are built in an automated fashion, using a process similar to that used for the other test series that are currently modeled. Post-processing scripts were also updated to compare the results of CTF to experimental data. The film and droplet measurements will be important to have for future activities in which the annular mist closure models and entrainment models will be further investigated. For this project, in which the wall drag model is being calibrated, the primary focus is on the two-phase pressure drop measurements. Results for the newly implemented test series are shown in Figs. 2 and 3 for Series 100 and 500, respectively. As with the FRIGG tests, the new flow regime map discussed in Section 3.4 was utilized for these tests.

Table 2. Summary of Riso test series

Series	Geometry	Outer diameter [mm]	Inner diameter [mm]	Length [m]	Heated
100	Annular	26	17	3.5	Yes
200	Tubular	10	—	9.0	No
300	Tubular	10	—	9.0	Yes
400	Tubular	10	—	9.0	Yes
500	Annular	26	17	8.0	No
600	Tubular	20	—	9.0	No

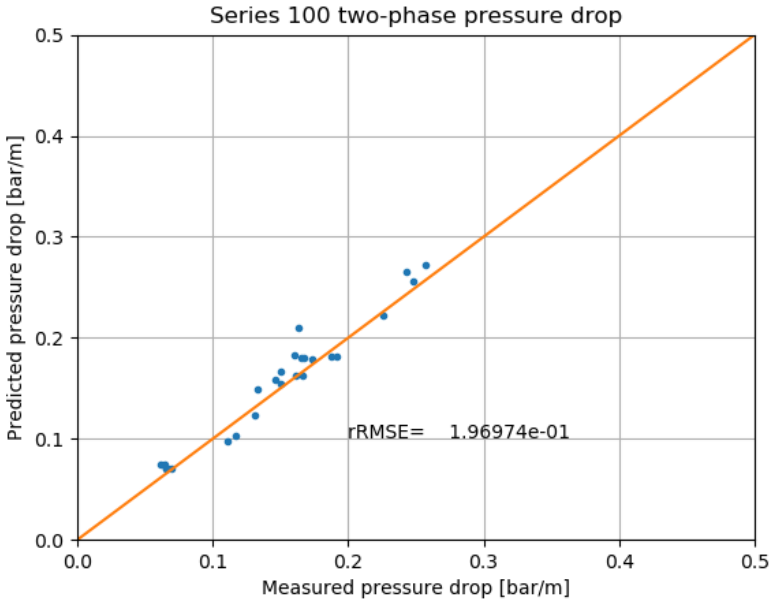

Figure 2. Comparison of CTF predictions to experimental data for Riso Series 100 tests.

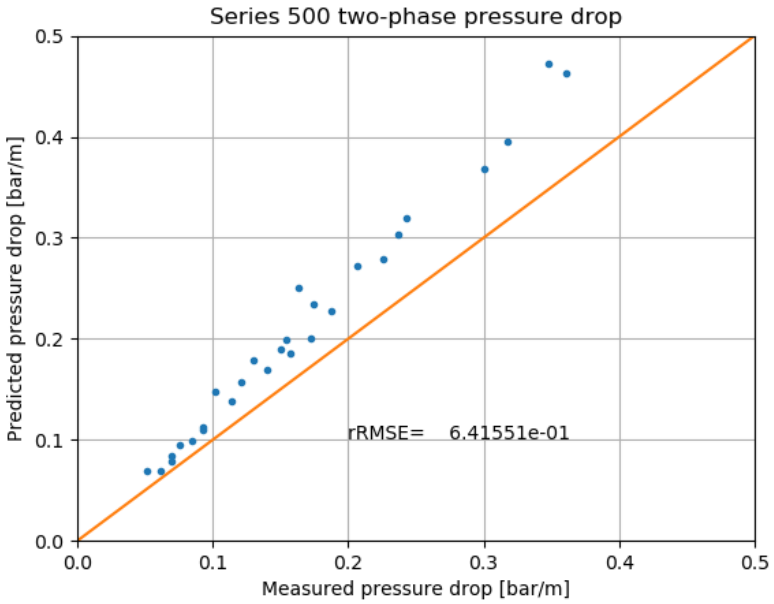

Figure 3. Comparison of CTF predictions to experimental data for Riso Series 500 tests.

3. MODEL IMPROVEMENTS

3.1 TWO-PHASE WALL SHEAR

The total wall shear can be calculated using a two-phase multiplier approach which relates the overall frictional pressure drop to an equivalent single phase flow:

$$\tau_w = \frac{\lambda_l}{2d_h}\frac{{G_m}^2}{\rho_l}\Phi_{tp}^2, \tag{1}$$

where Φ_{tp}^2 is the two-phase flow multiplier, λ_l is the single phase liquid friction factor, d_h is the hydraulic diameter, and G is the total (mixture) mass flux, defined as

$$G_m = \alpha_\ell \rho_l v_\ell + \rho_v \alpha_v v_v + \rho_e \alpha_e v_e. \tag{2}$$

In the equation, α, ρ, and v represent volume fraction, density, and velocity, and the three subscripts—ℓ, v, and e—represent the three fields solved by CTF, which are liquid, vapor, and droplets. The Chisholm model is a quality-based two-phase multiplier model and is derived for evaporating flow. In the Chisholm model, a simplified set of conservation equations are solved to obtain an analytical expression for the two-phase pressure drop gradient Chisholm [1973]. The pressure gradient is defined as if the whole mixture flows is liquid or vapor for both phases, as follows:

$$\left(\frac{dP}{dX}\right)_{\text{fric}}^{\ell\text{o}} = \frac{f_{\ell\text{o}}}{2d_h}\frac{{G_m}^2}{\rho_\ell} \tag{3}$$

$$\frac{dP}{dX}\Big)_{\text{fric}}^{\text{vo}} = \frac{f_{\text{vo}}}{2d_h}\frac{{G_m}^2}{\rho_v}. \tag{4}$$

The linear pressure drop is denoted with $\frac{dP}{dx}$, where P is the pressure, and x represents the axial length. As indicated by the "fric" subscript, the Chisholm model is solving for wall shear only. The $f_{\ell\text{o}}$ and f_{vo} are liquid-only and vapor-only friction factors, respectively, and they are functions of the total (mixture) mass flux. Defining the physical property coefficient, Γ as

$$\Gamma^2 = \frac{\left(\frac{dP}{dX}\right)_{\text{fric}}^{\ell\text{o}}}{\frac{dP}{dX}\Big)_{\text{fric}}^{\text{vo}}}, \tag{5}$$

and substituting Eqs. (4) and (3) into Eq. (5) leads to

$$\Gamma = \left(\frac{\rho_\ell}{\rho_v}\right)^{0.5}\left(\frac{f_{\text{vo}}}{f_{\ell\text{o}}}\right)^{0.5}. \tag{6}$$

Finally, the Chisholm two-phase flow multiplier expression is given as

$$\Phi_{\ell o}^2 = 1 + \left(\Gamma^2 - 1\right)\left(B x_{\text{flow}}\left(1 - x_{\text{flow}}\right) + x_{\text{flow}}^2\right). \tag{7}$$

The flow quality is given by x_{flow} and B is defined as

$$B = \frac{C\Gamma - 2}{\Gamma^2 - 1}. \tag{8}$$

C is a constant given by

$$C = \left(\frac{v_\ell}{v_g}\right)\left(\frac{\rho_\ell}{\rho_v}\right)^{0.5} + \left(\frac{v_v}{v_\ell}\right)\left(\frac{\rho_v}{\rho_\ell}\right)^{0.5}. \tag{9}$$

It must be noted that the Chisholm two-phase flow multiplier satisfies the boundary condition at the limits of single-phase liquid $x = 0$ and single-phase vapor $x = 1$. This can be easily verified by substituting the limiting values in Eq. (7).

Fig. 4 shows the comparison for the two-phase pressure drop prediction for the Risø dataset between the base Wallis and Chisholm models with stable film enabled. While there is a reduction in the root mean squared error (RMSE) and the mean error with the Chisholm model, a consistent under-prediction of the two-phase pressure drop is observed, especially for higher measured pressure drops. The Risø dataset can be used to calibrate the model coefficients, which is further discussed in Section 4..

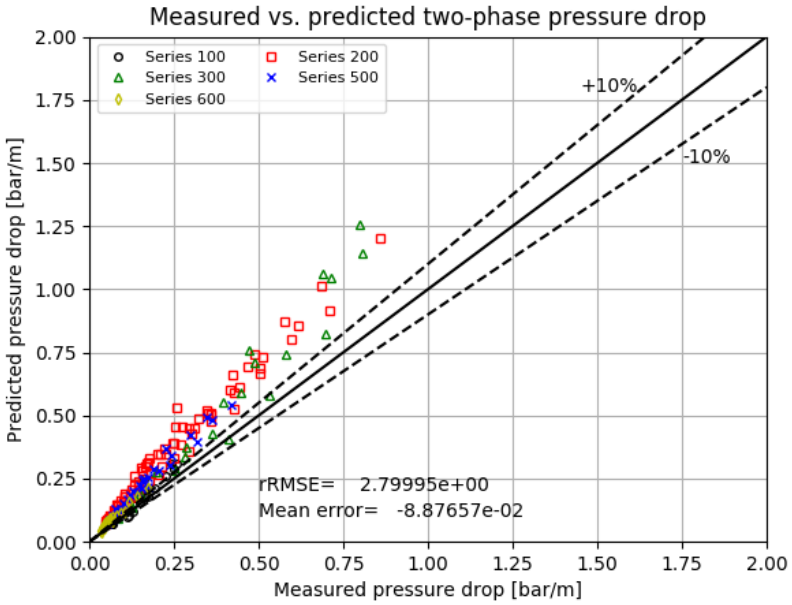

(a) Base Wallis model

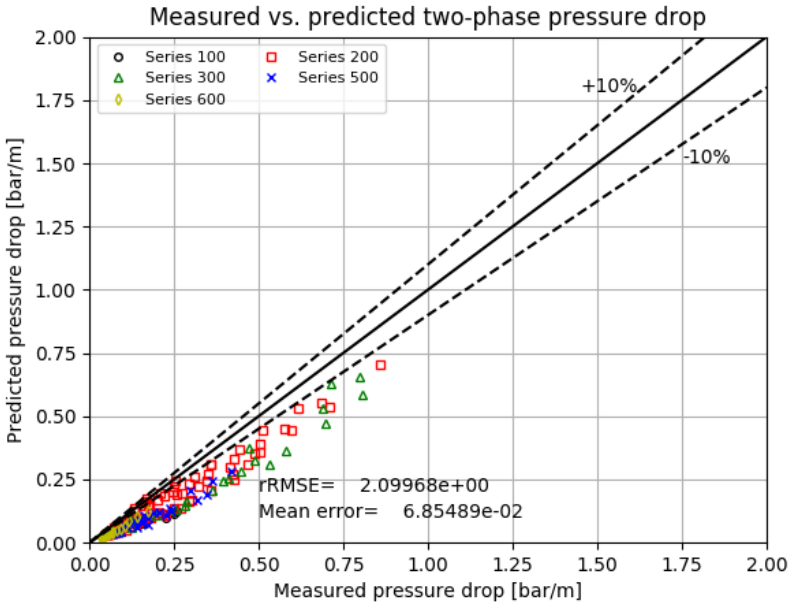

(b) Chisholm model

Figure 4. Risø comparison of predicted and measured two-phase pressure drop with the base Wallis and Chisholm models with stable film enabled.

3.2 WALL HEAT TRANSFER

The wall heat transfer model in the subcooled nucleate boiling regime is based on one of two approaches which are hereby titled (1) the Hancox-Nicoll approach and (2) the Saha-Zuber approach. The Hancox-Nicoll approach is the base subcooled boiling wall heat partitioning model in CTF, and it is described in detail in the CTF Theory manual Salko et al. [2017a] as *Approach 1: Non-ONB model*. According to the Hancox-Nicoll approach, the heat transfer from the wall to the liquid is divided into three components: forced convection to the liquid, vapor generation at the wall, and condensation of bubbles at the wall. The near-wall condensation heat transfer accounts for the heat flux of the condensing bubbles which returns to the liquid, and its value is required to determine the ratio of latent heat to sensible heat transfer from the wall to the fluid. The Saha-Zuber approach is documented in the Theory Manual as Approach 2, and it was implemented as part of the previous milestone (Salko et al. [2020b]). In this approach, heat transfer is still divided into forced convection and vapor generation at the wall; however, there is no explicit near-wall condensation term. Instead, the critical enthalpy required for the start of vapor generation is used to capture this effect. Upon further review of this new model, several improvements were implemented as part of this work. First, the pumping term, which is calculated by the Rouhani model (Rouhani and Axelsson [1970]) and accounts for the energy required for reheating the thermal boundary layer when the departing vapor bubble is replaced by subcooled liquid, was removed from this model, because the effect is implicitly captured in the Gorenflo heat transfer model. Inclusion of the pumping term will lead to an under-prediction in void generation. Therefore, in this approach, the effective vapor generation fraction is now calculated as follows:

$$F_{\text{gam}} = \frac{h_\ell - h_{\text{cr}}}{h_f - h_{\text{cr}}}. \tag{10}$$

In the equation, h_{cr} represents the critical enthalpy required for bubble detachment, which is determined from the Saha-Zuber correlation.

A second improvement was made to address how the boiling heat flux is converted to the boiling heat transfer coefficient (HTC) required by the CTF solid conduction equation solution. First, the Gorenflo Gorenflo and Kenning [1993] pool boiling heat flux is restated here for clarity and can be expressed as follows:

$$q''_{\text{pb}} = \left(\frac{h_o F(p^*) \left(T_{\text{w}} - T_{\text{sat}}\right)}{q''^{n}_{o}} \right)^{1/(1-n)}, \tag{11}$$

where h_{o} is the reference heat transfer coefficient, $F(\text{p}^*)$ is the influence of the reduced pressure where p^* is the reduced pressure, F_{w} is the influence of wall properties, and the wall heat flux factor is defined in terms of the reference heat flux, q''_{o}, where n is a function of the reduced pressure. This is converted to an HTC by dividing by the temperature difference between wall and fluid which, in the case of boiling, shall be the wall temperature minus the saturation temperature. Currently, the difference between rod surface temperature and the saturation temperature, ΔT_{sat}, is erroneously calculated in the code based on the temperature difference between the superheated wall and the subcooled liquid temperature. It must be emphasized here that the temperature difference should be the wall superheat (ΔT_{sat}) in both the subcooled and superheated regimes.

A third improvement to this model is that the numerical derivative of the heat transfer correlation with respect to the rod surface temperature (also required for the solid conduction equation boundary condition), has been replaced by an analytical derivative, as follows:

$$\frac{dHTC}{dT_{\mathrm{s}}} = \left(q_{pb} - q_{bi}\right)^2 \left(q_{fc}^3 + \left(q_{pb} - q_{bi}\right)^3\right)^{-\frac{2}{3}} \left(\frac{q_{pb}}{{\Delta T_{\mathrm{s}}}^2}\right)\left(\frac{1}{1-n}\right) - \left(\frac{q_{nb}}{{\Delta T_{\mathrm{s}}}^2}\right), \tag{12}$$

where q_{bi} is the pool boiling heat flux at the point of boiling initiation. A final correction was made to the critical enthalpy model itself. According to the original model, in the calculation of the enthalpy of detachment of the vapor bubble, h_{cr}, the total wall heat flux, q_{w}" must be used instead of the effective nucleate/pool boiling heat flux, as done previously. This has been corrected as follows:

$$h_{\mathrm{cr}} = h_{\mathrm{f}} - \frac{\left(q''_{\mathrm{w}} D_h C p_f\right)}{(k_l.Pe.St)}, \tag{13}$$

where Pe is the Peclet number, and St is the Stanton number. The results using these model modifications are presented in Section 3.4.

3.3 PHASE HEAT TRANSFER

Phase heat transfer refers to the energy transferred from one phase to another as the result of evaporation or condensation. This includes both mass and energy transfer between the phases, because it is driven by a mass transfer. Furthermore, the phase change/energy transfer that results from boiling on heated surfaces is also included in this model. The original model in CTF is shown in Eq. 14:

$$\Gamma_{\text{net}} = \left[\Gamma_{\text{evap,shl}} + \Gamma_{\text{evap,shv}} + \Gamma_{\text{boil}}\right] - \left[\Gamma_{\text{cond,scl}} + \Gamma_{\text{cond,scv}}\right]. \tag{14}$$

In the equation, Γ_{net} is the mass transfer from liquid to vapor. There are four Γ terms that account for mass transfer due to implicit heat transfer (energy exchange at the liquid/vapor interface). The four terms have subscripts that are a combination of *evap*/*cond*, which stands for *evaporation* or *condensation*, and *shv*/*shl*/*scv*/*scl*, which stand for *superheated vapor*, *superheated liquid*, *subcooled vapor*, and *subcooled liquid*. These four terms are defined in the following equation array:

$$\begin{aligned}
\Gamma_{\text{evap,shl}} &= \frac{h_{\text{int,shl}}}{(h_g - h_l)C_{p,l}}|h_l - h_f| \\
\Gamma_{\text{evap,shv}} &= \frac{h_{\text{int,shv}}}{(h_g - h_l)C_{p,v}}|h_v - h_g| \\
\Gamma_{\text{cond,scl}} &= \frac{h_{\text{int,scl}}}{(h_v - h_f)C_{p,l}}|h_l - h_f| \\
\Gamma_{\text{cond,scv}} &= \frac{h_{\text{int,scv}}}{(h_v - h_f)C_{p,v}}|h_v - h_g|.
\end{aligned} \tag{15}$$

The h_{int} terms represent the interfacial HTC between the phases. There is one term defined for each possible condition (superheated or subcooled and vapor or liquid). These terms are flow-regime dependent, as they depend on the structure of the two-phase flow. An assessment of the closure models used for these terms was not performed for this report; however, these terms are defined in more detail in the CTF Theory Manual Salko et al. [2017a]. Other terms in these equations include C_p (the specific heat for both liquid, l, and vapor, v) and the enthalpy, h, which can be for the saturated liquid (subscript f), saturated vapor (subscript g), or the actual enthalpy (h_l for liquid and h_v for vapor). The product of C_p and the enthalpy difference is the same as a temperature difference which, when multiplied by the interfacial HTC, results in a heat flux. When this heat flux is divided by the latent heat of vaporization ($h_g - h_f$), it results in a mass transfer rate. Note that CTF is coded in such a way that two of these terms will be zero, depending on whether the fluid is super-heated or sub-cooled, as a fluid cannot be in both conditions simultaneously.

The final term which to be defined from Eq. 14 is the wall boiling vapor generation, Γ_{boil}. This term specifically covers vapor generated at the wall due to surface boiling. CTF will calculate a boiling heat flux for the surface which subtracts vapor that condenses in the near-wall region due to subcooling effects. This term will be divided by the energy increase required to change the subcooled liquid to a saturated vapor or $h_g - h_l$ to obtain the Γ_{boil} term.

Note that there were three errors in the original implementation of this model. First, there was no C_p term in the calculation of $\Gamma_{\text{evap,shl}}$ or $\Gamma_{\text{cond,scl}}$. The authors assume that the original developers assumed that the

Table 3. Summary of change in test statistics (comparison of CTF and void validation tests) after implementing corrections to the phase change model.

Test	Mean void error ($1\times1\cdot10^{-2}$)	
	Original	Corrected
PSBT Series 1	7.0	4.6
PSBT Series 2	5.4	4.3
PSBT Series 3	6.9	4.3
PSBT Series 4	2.4	2.5
PSBT Series 5	2.9	-0.6
PSBT Series 6	2.7	-0.4
PSBT Series 7	8.0	4.0
BFBT bundle	4.9	3.7

specific heat can be unity, so this term can be dropped. However, the specific heat will not be exactly unity for all conditions, and it is already being considered for the vapor phase, so for consistency and correctness, the term was added back. Second, the enthalpy change of the fluid (the terms in the absolute value operations) were coded as the latent heat of vaporization. This is not strictly correct, because the fluid can be either subcooled or superheated, resulting in a larger temperature difference between the fluid and interface. Therefore, these terms were modified as presented in Eq. 14. Third, and most importantly, a double-counting of the Γ_{boil} term was discovered in the calculation. This meant that the vapor generation due to wall boiling was being doubled. After correcting all three of these issues, the validation matrix was re-run. Results for the void measurement cases are presented in the remainder of this section. The comparisons of the PWR subchannel and bundle tests (PSBT) single-channel cases are shown in Figs. 5–8. The comparisons of the PSBT bundle cases are shown in Figs. 9–11. The comparisons of the BFBT bundle void measurement cases are shown in Fig. 12 for all measurement points. The data are collapsed down to a single area-weighted void for the entire bundle in Fig. 13 to allow for easier visualization of the trend.

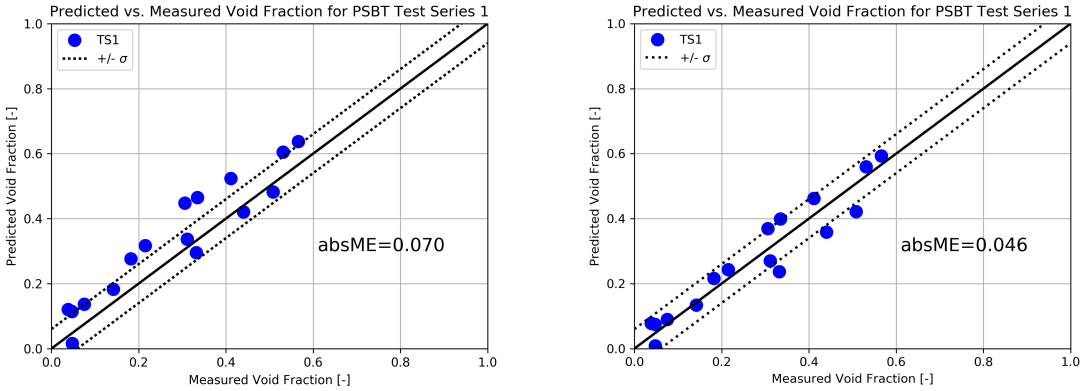

(a) Original model. **(b) Corrected model.**

Figure 5. PSBT Series 1 comparison of predicted and measured void before and after correction of the phase mass transfer model.

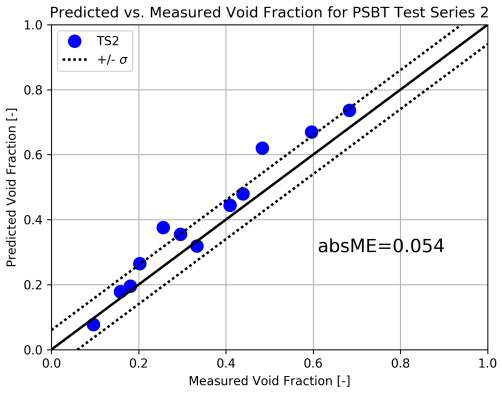

(a) Original model.

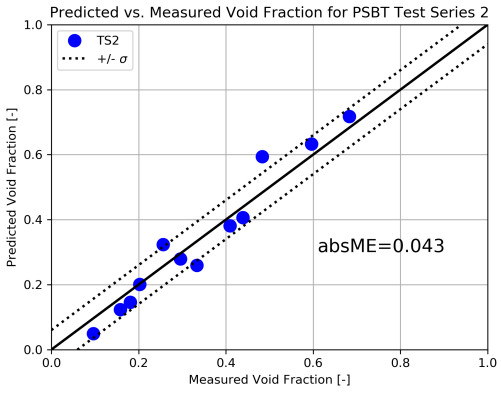

(b) Corrected model.

Figure 6. PSBT Series 2 comparison of predicted and measured void before and after correction of the phase mass transfer model.

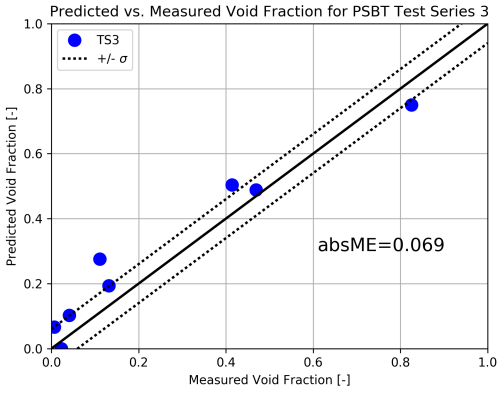

(a) Original model.

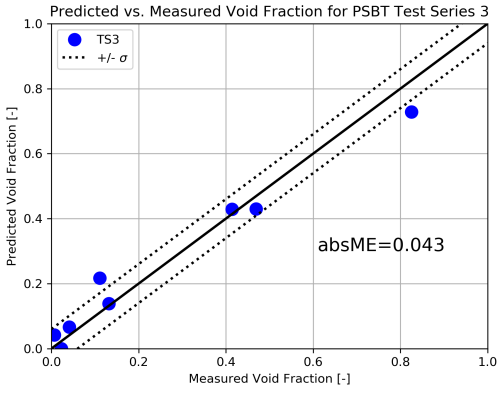

(b) Corrected model.

Figure 7. PSBT Series 3 comparison of predicted and measured void before and after correction of the phase mass transfer model.

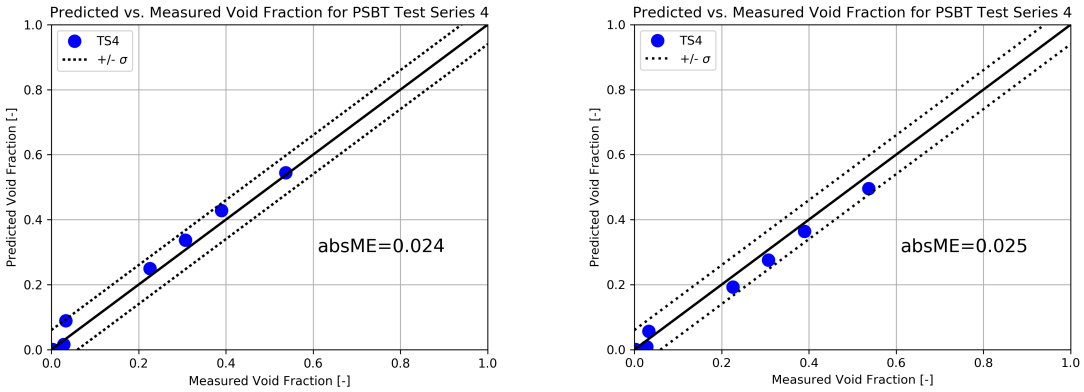

(a) Original model. **(b) Corrected model.**

Figure 8. PSBT Series 4 comparison of predicted and measured void before and after correction of the phase mass transfer model.

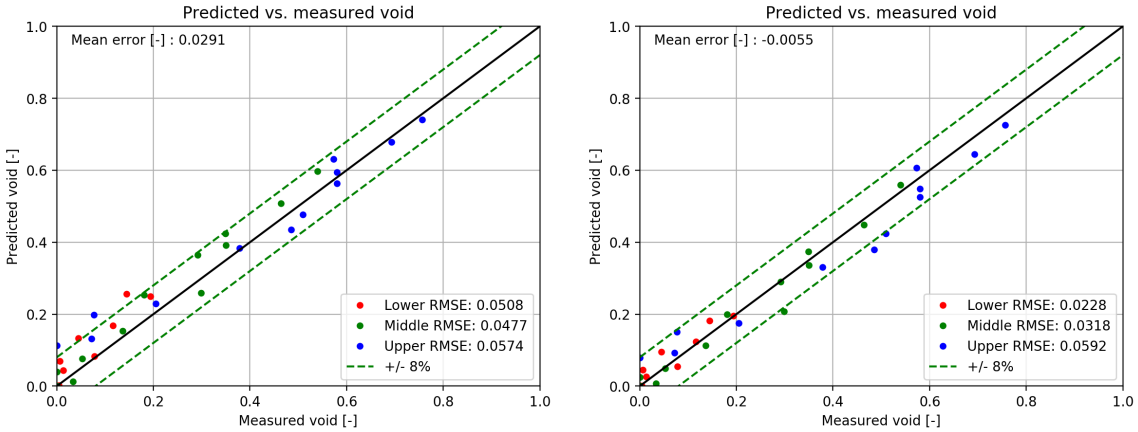

(a) Original model. **(b) Corrected model.**

Figure 9. PSBT Series 5 comparison of predicted and measured void before and after correction of the phase mass transfer model.

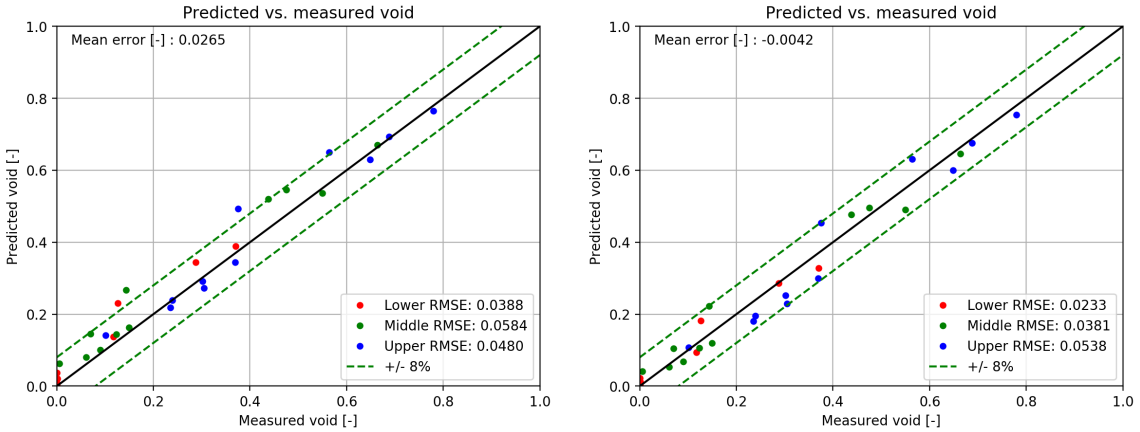

(a) Original model. **(b) Corrected model.**

Figure 10. PSBT Series 6 comparison of predicted and measured void before and after correction of the phase mass transfer model.

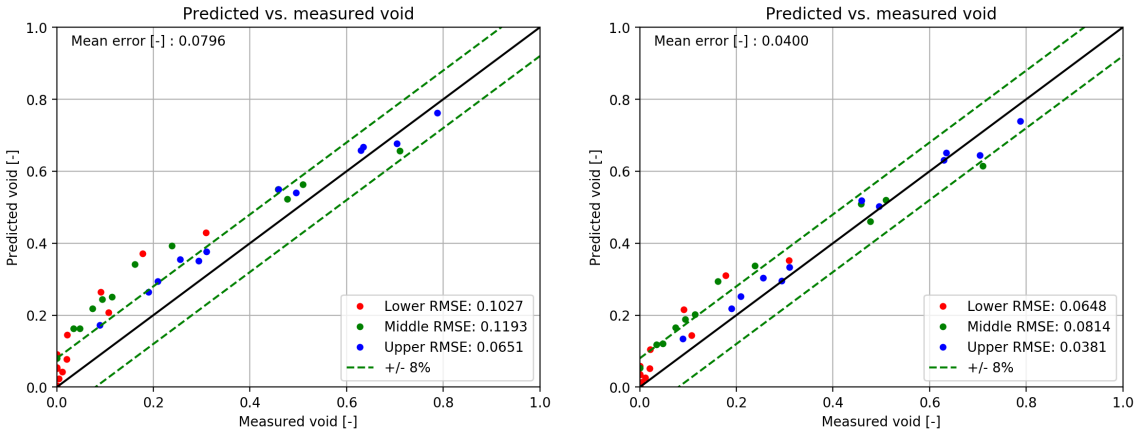

(a) Original model. **(b) Corrected model.**

Figure 11. PSBT Series 7 comparison of predicted and measured void before and after correction of the phase mass transfer model.

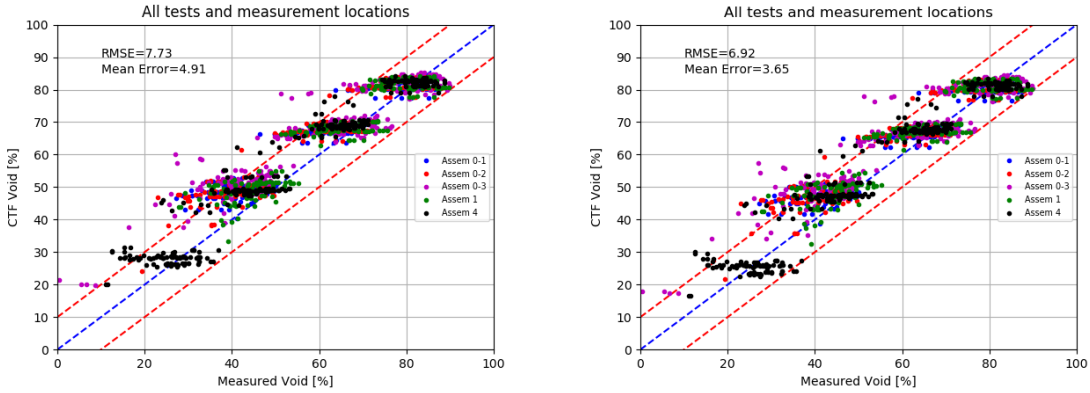

(a) Original model. **(b) Corrected model.**

Figure 12. BFBT bundle comparison of predicted and measured void before and after correction of the phase mass transfer model.

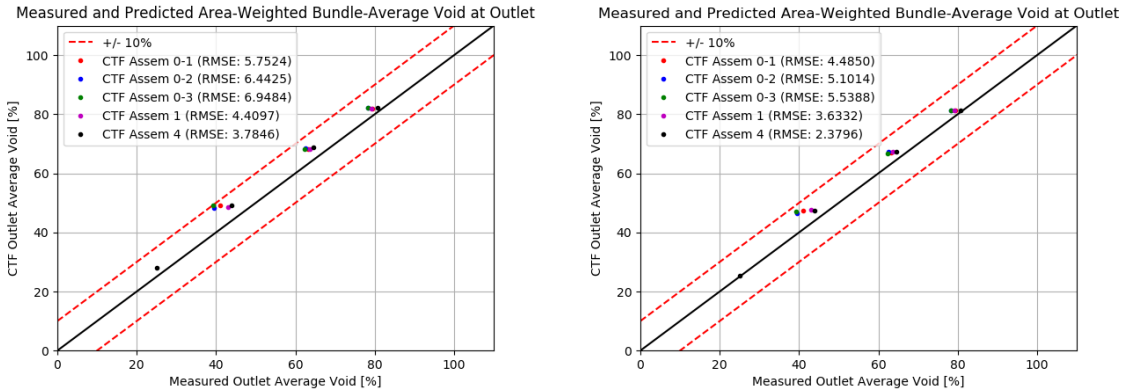

(a) Original model. **(b) Corrected model.**

Figure 13. BFBT bundle comparison of predicted and measured area-weighted void before and after correction of the phase mass transfer model.

3.4 FLOW REGIME MAP

The internal structures of two-phase flow are classified by the flow regimes or flow patterns. The flow regime identification is important in a two-phase flow analysis, because constitutive equations are heavily dependent on the two-phase flow geometry and behavior. For instance, in a critical power calculation, the accuracy of dryout predictions depends to a large extent on the initial conditions of the film, which is sensitive to the point at which the transition to annular flow starts. The flow regime behavior is strongly dependent upon physical properties, flow conditions, flow orientation, channel geometries, and channel size. The legacy CTF flow regime map classified the flow regime into four distinct flow regimes, including small bubble, slug, churn turbulent or transition flow, and annular mist flow regime, as indicated in Table 4. The transition to annular flow is defined by Eq. 16. Testing of the code indicated that this expression tends to push the transition to annular flow to unrealistically high values of 0.9 or larger for prototypical BWR conditions:

$$\alpha_{\text{crit}} = \max \begin{cases} 1 - \dfrac{2\sigma}{\rho_v |v_{v\ell}|^2 D_h} - \alpha_\ell \\ \\ 0.8 \end{cases} \tag{16}$$

Table 4. CTF legacy flow regime map

Flow regime	Criteria
Small bubble	$0 < \alpha \leq 0.2$
Small-to-large bubble	$0.2 < \alpha \leq 0.5$
Churn/turbulent	$0.5 < \alpha \leq \alpha_{\text{crit}}$
Annular/mist	$\alpha_{\text{crit}} < \alpha \leq 1.0$

In this equation, σ is the surface tension, and α_ℓ is the liquid volume fraction. To improve this, the model was replaced with a more physically correct model inspired from GEH [2008]. The criteria in this model are established based on when the liquid in the film can be lifted by the vapor flow relative to the liquid in the churn flow regime. Following the same nomenclature as that presented in GE [2008], the velocity in bubbly flow is defined by the drift flux model as follows:

$$V_{g,bc} = C_{0,bc} j + \overline{V}_{gj,bc}, \tag{17}$$

with the distribution parameter $C_{0,bc}$ and drift velocity $\overline{V}_{gj,bc}$ defined as:

$$\begin{aligned} C_{0,bc} &= C_{\infty,bc} - (C_{\infty,bc} - 1) \sqrt{\frac{\rho_v}{\rho_\ell}} \\ C_{\infty,bc} &= 1.288 + 0.105 \left(4.5 \sqrt{\frac{\rho_v}{\rho_\ell}} \right) - 0.0015 log\,(Re_l) \end{aligned} \tag{18}$$

$$\overline{V}_{gj,bc} = k\left(\frac{\sigma\Delta\rho g}{\rho_\ell^2}\right)^{\frac{1}{4}}, \tag{19}$$

where Re_ℓ is the liquid Reynolds number defined as $\frac{GD_h}{\mu_\ell}$, and k is a constant set to 1.53. The $J = (1-\alpha_v)\,v_\ell + \alpha_v v_v$ is the total volumetric flux. Note that this constant must be consistent with the drift velocity used in the derivation of the drag that is also used in the calculation of the interface heat transfer. At this stage, they are different, but in the future, the calibration tools will be used to improve this constant's agreement to void data and to consolidate its use for all models. Similarly, for annular flow, we have

$$V_{g,an} = C_{0,an} j + \overline{V}_{gj,an}, \tag{20}$$

with $C_{0,an}$ and $\overline{V}_{gj,bc}$ for pure annular flow (no droplet in the core), defined as:

$$C_{0,an} = 1 + \frac{(1-\alpha_v)}{\alpha_v + \sqrt{\frac{1+75(1-\alpha_v)}{\sqrt{\alpha_v}}}\sqrt{\frac{\rho_v}{\rho_\ell}}}, \tag{21}$$

$$\overline{V}_{gj,an} = \frac{(1-\alpha_v)}{\alpha_v + \sqrt{\frac{1+75(1-\alpha_v)}{\sqrt{\alpha_v}}}\sqrt{\frac{\rho_v}{\rho_\ell}}\sqrt{\frac{\Delta\rho g D_H(1-\alpha_v)}{0.015\rho_\ell}}}. \tag{22}$$

According to Ishii Mishima and Ishii [1987], the expression $\sqrt{\frac{1+75(1-\alpha_v)}{\sqrt{\alpha_v}}}\sqrt{\frac{\rho_v}{\rho_\ell}}$ is approximately 4 for $\frac{\rho_v}{\rho_\ell} << 1$. With this simplification, equations (21) and (22) can be reduced to

$$C_{0,an} = 1 + \frac{(1-\alpha_v)}{\alpha_v + 4\sqrt{\frac{\rho_v}{\rho_\ell}}} \tag{23}$$

$$\overline{V}_{gj,an} = \frac{(1-\alpha_v)}{\alpha_v + 4\sqrt{\frac{\rho_v}{\rho_\ell}}}\sqrt{\frac{\Delta\rho g D_H\,(1-\alpha_v)}{0.015\rho_\ell}}. \tag{24}$$

As indicated above, the transition to annular flow is defined by the intersection of Eqs. (21) and (22), and this translates to

$$C_{0,bc} j + \overline{V}_{gj,bc} = C_{0,an} j + \overline{V}_{gj,an}. \tag{25}$$

Substituting Eq. (23) and (24) into (25), the result is

$$C_{0,bc} j + \overline{V}_{gj,bc} = \left(1 + \frac{(1-\alpha_v)}{\alpha_v + 4\sqrt{\frac{\rho_v}{\rho_\ell}}}\right) j + \frac{(1-\alpha_v)}{\alpha_v + 4\sqrt{\frac{\rho_v}{\rho_\ell}}}\sqrt{\frac{\Delta\rho g D_H\,(1-\alpha_v)}{0.015\rho_\ell}}. \tag{26}$$

In the $\overline{V}_{gj,an}$, the term $\sqrt{(1-\alpha_v)}$ must be simplified to allow for an analytical solution of the α_v. Otherwise, it becomes necessary to solve for it numerically, which is not practical because it adds time to the overall solution. One approximation is to replace the void with the $\alpha_v = 0.7$, which is a suitable approach for the annular transition ranging from 0.6 to 0.75. With this, $\sqrt{(1-\alpha_v)} \approx 0.5$, and Eq. (26) reduces to

$$C_{0,bc}\, j + \overline{V}_{gj,bc} = \left(1 + \frac{(1-\alpha_v)}{\alpha_v + 4\sqrt{\frac{\rho_v}{\rho_\ell}}}\right) j + \frac{(1-\alpha_v)}{\alpha_v + 4\sqrt{\frac{\rho_v}{\rho_\ell}}} 0.5 \sqrt{\frac{\Delta\rho g D_H}{0.015\rho_\ell}}. \tag{27}$$

Multiplying both sides with $\left(\alpha_v + 4\sqrt{\frac{\rho_v}{\rho_\ell}}\right)$ gives

$$\left(C_{0,bc}\, j + \overline{V}_{gj,bc}\right)\left(\alpha_v + 4\sqrt{\frac{\rho_v}{\rho_\ell}}\right) = \left(\alpha_v + 4\sqrt{\frac{\rho_v}{\rho_\ell}} + (1-\alpha_v)\right) j + 0.5\,(1-\alpha_v)\sqrt{\frac{\Delta\rho g D_H}{0.015\rho_\ell}}. \tag{28}$$

Rearranging this equation and solving for α_v leads to the final form of the GE transition to annular flow correlation:

$$\alpha_{trans} = \frac{j + 4\sqrt{\frac{\rho_v}{\rho_\ell}}\left((1-C_{0,bc})\, j - 1.53\left(\frac{\sigma\Delta\rho g}{\rho_\ell^2}\right)^{\frac{1}{4}}\right) + 0.5\sqrt{\frac{\Delta\rho g D_H}{0.015\rho_\ell}}}{C_{0,bc}\, j + 1.53\left(\frac{\sigma\Delta\rho g}{\rho_\ell^2}\right)^{\frac{1}{4}} + 0.5\sqrt{\frac{\Delta\rho g D_H}{0.015\rho_\ell}}}. \tag{29}$$

It is noted that Eq. (29) differs from that published in the TRACG Model Description GE [2008]. The General Electric (GE) published correlation includes a negative sign in the denominator for the annular flow drift flux velocity, which is incorrect. The correlation behavior was compared to that presented in other published correlations, including the Steen Wallis correlation for the same geometry and thermal hydraulic conditions at a pressure of 70 bar and mass flux of 1,000 $\mathrm{kg\,m^{-2}\,s^{-1}}$. The results of this comparison are depicted in Fig. 14. In this figure, the red curve is the void vs. quality predicted by the drift flux bubbly churn flow model, whereas the black curve is obtained by the drift flux annular model. The transition to annular flow is defined as the point of intersection of these two curves, which is given by Eq. (29). The point of intersection is highlighted by the vertical dashed line, which corresponds to the coordinates (quality, void) of (0.21, 0.7). On the other hand, the Steen Wallis correlation is shown by a straight vertical line for a quality of 0.15, which is approximately 0.6 in void fraction. This is lower than that predicted by Eq. (29), but it is in line with the lower end of the GE transition to annular flow expressed by Eq. (29) minus 10% from the transition region ($(\alpha_{trans} - 0.1)$). It shall be noted here that this example only highlights how the correlation works; the main assessment of the flow regime map should be performed in connection with the interfacial shear model based on the accuracy of void fraction prediction. After making the implementation, test cases for validation of bundle average void fraction were rerun, and a comparison was performed between the baseline and improved CTF models. The baseline models included the Thom model for subcooled boiling, the Hancox-Nicoll model for condensation, the Wallis model for the annular mist interfacial friction, the legacy interfacial drag models, and the legacy flow regime map. The improved CTF models included onset of nucleate boiling (ONB), Saha-Zuber, and Gorenflo for the subcooled boiling model, Wallis with stable film only for the interfacial shear friction,

drift flux interfacial drag models, and the GE flow regime map. The only objective for this comparison is to show the bundle average void fraction, since void drift and mixing have not yet been reviewed.

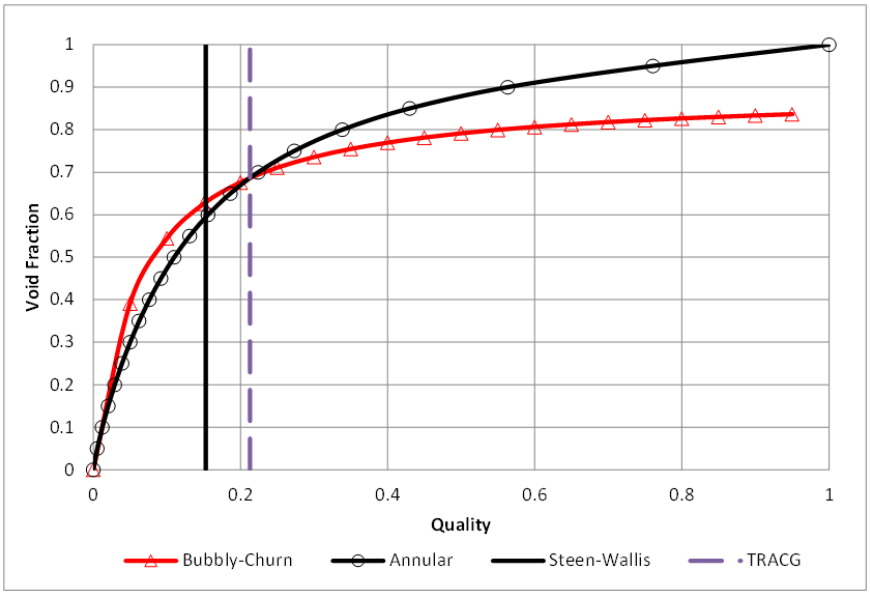

Figure 14. TRACG transition to annular flow in comparison to Steen Wallis correlation

The comparison of the PSBT is shown in Fig.15. The figure presents void prediction results for baseline and enhanced CTF. The overall comparison statistics, the mean error calculated as the average of the difference between predicted and measured data, and the RMSE are also shown in the upper left corner of the plot. As indicated, CTF with baseline models overpredicted void by 3.16%, but this was dropped to -.92% with the improved models. Figure 16 summarizes statistics comparison prediction of CTF with the enhanced model, CTF with baseline models, and other subchannel codes such as VIPRE-01 and F-COBRA-TF (AREVA). Results were obtained from PSBT benchmark results psb [2016.] and Zhao (VIPRE-01 (ORNL)) Zhao et al. [2019.]. As indicated by the figure, the baseline CTF results were overpredicting void by a considerable margin, particularly for S1, S2, and S3 geometries and the results were significantly different than those obtained using other popular codes used in the nuclear industry. Inclusion of the new closure models has helped to significantly reduce the CTF bias, bringing its void estimation in line with other popular T/H codes.

For the PSBT 5×5 bundle test series results, predicted versus the measured average void fraction are presented, along with the statistics in Fig. 17. As can bee seen, and as expected, CTF (Base) overpredicts the data, particularly in the bubbly/slug flow, whereas the results agree with the data in the transition-to-annular-flow region. For the CTF (Enhanced), the bubbly/slug flow void prediction improved, but the code slightly underpredicted the void in the transition-to*annular-flow region. Overall, in terms of the void error calculated as predicted minus measured, CTF (Enhanced) performs better than CTF (Base). Figure 18 summarizes a statistical evaluation comparison for the mean error and RMSE per geometry type between CTF (Base) and CTF (Enhanced). As indicated, the agreement is quite good for both CTF (base) and CTF (Enhanced), with an average percentage error generally less than 2% for geometries S5 and S6. It is noted here that CTF (Base) overpredicts data, and CTF (Enhanced) underpredicts data, with slightly better prediction for CTF (Enhanced). For S7 geometry, it is observed that CTF (Base) overpredicts data by

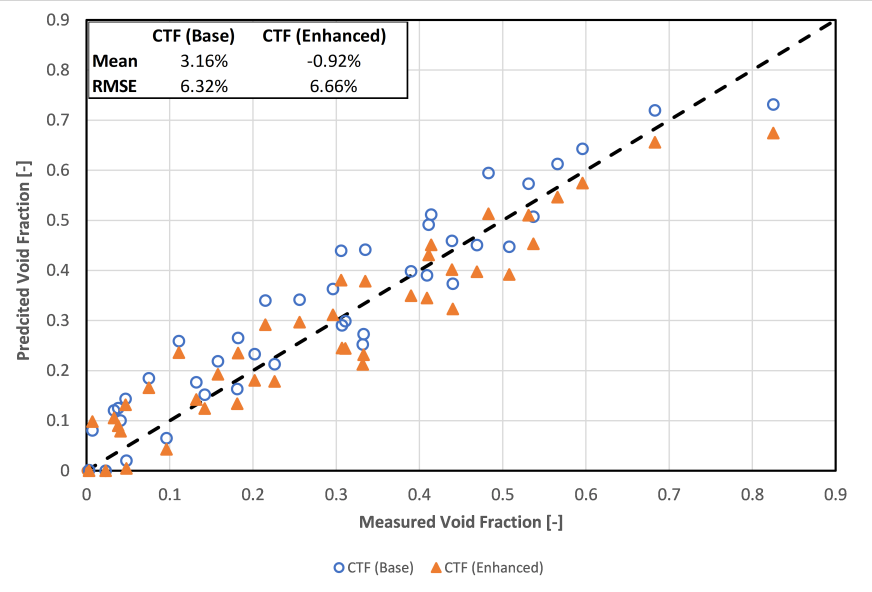

Figure 15. Comparison of CTF predictions of PSBT single channel void using legacy models compared with improved models (flow regime map, phase change, and wall heat transfer).

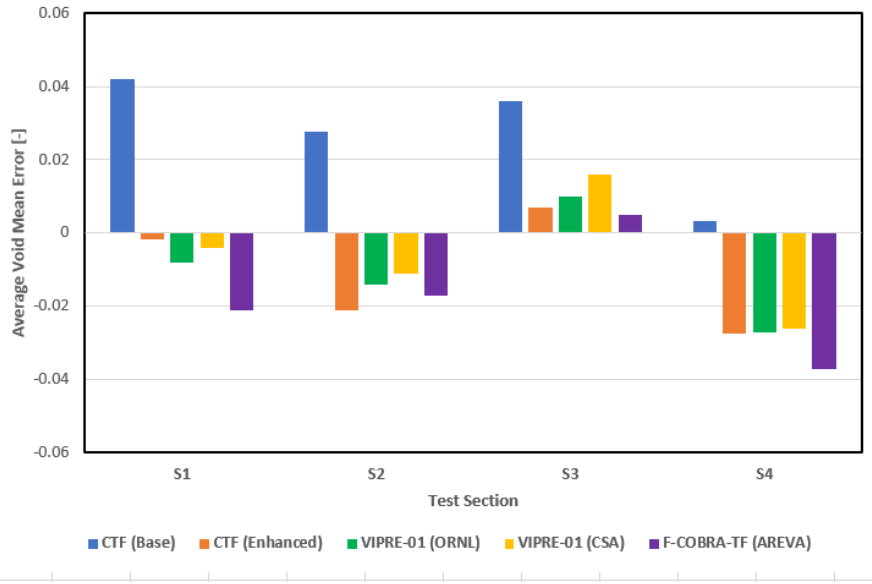

Figure 16. Comparison of CTF predictions of PSBT single channel void using legacy models, improved models (flow regime map, phase change, and wall heat transfer), and benchmarking against other T/H codes.

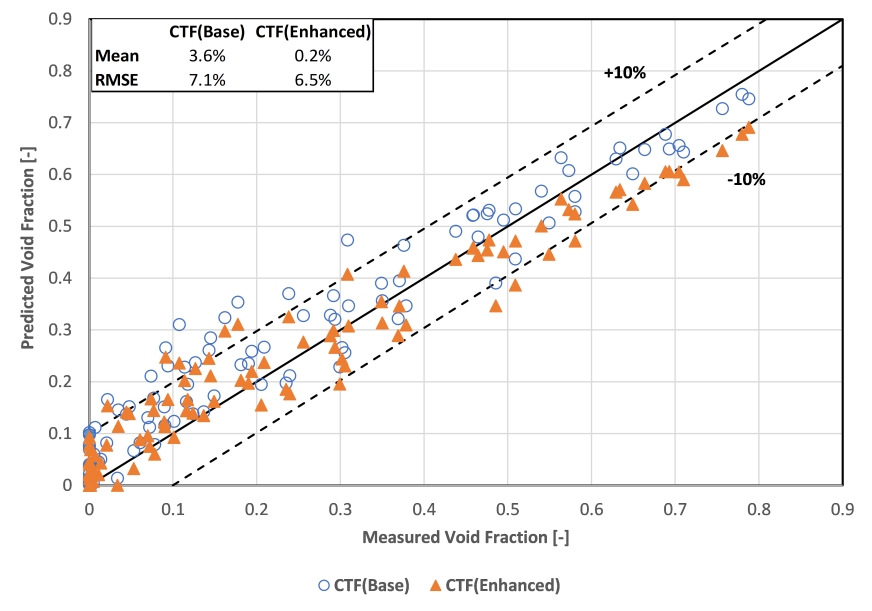

Figure 17. Comparison of PSBT 5×5 bundle test measured void and CTF when using legacy models compared to improved models (flow regime map, phase change, and wall heat transfer).

as much as 7.2%, whereas in CTF (Enhanced), overprediction was reduced to only 3.2%.

The comparison to the BFBT outlet void fraction, along with the overall statistics, are shown in Fig. 19. Overall, it can be seen that agreement with the data obtained using CTF (Enhanced) is better than that obtained when using CTF (Base). The accuracy of CTF (Enhanced) prediction is comparable to the accuracy of experimental uncertainties, which is typically 2% for bundle average void fraction. Figure 20 summarizes the statistics of the CTF (Base) and CTF (Enhanced) mean void average error evaluated at each flow regime and calculated as predicted-minus-measured. The slug and bubbly flow in this figure is represented by outlet void below 63%, whereas annular region is considered for void above 75%. As indicated in this figure, the overprediction at the 40% level was essentially eliminated by switching to CTF (Enhanced) models. The same behavior is also observed at the churn-turbulent regime, which is a linear combination of interfacial drag values calculated for the annular mist and slug flow regimes. For 75% void level, which is mostly annular mist flow, the overprediction with CTF (Base) version was slightly reduced from the CTF (Enhanced) version, but with the same accuracy. This suggests that the interfacial shear still high and needs to be reduced. At void below 30%, the CTF (Enhanced) version underpredicted the void; this is likely caused by the empirical nature of the Ishii correction to the distribution parameter in the subcooled boiling situation, which does not involve subchannel local conditions that reflect the physics of the problem.

For the FRIGG data, the calculated average bundle void fraction was compared with the measured data with both CTF (Base) and CTF (Enhanced). The results of the comparison, along with the statistics, are shown in Fig. 21a. As seen in this figure, overall, the CTF (Base) version overpredicted the void fraction, which is consistent with that observed for other benchmark tests. With the CTF (Enhanced) version, it can be seen that up to a void fraction of 40%, the code agrees very well with the data; however, above 40%, the code tends to slightly under-predict the void fraction, particularly at the transition to annular flow. This

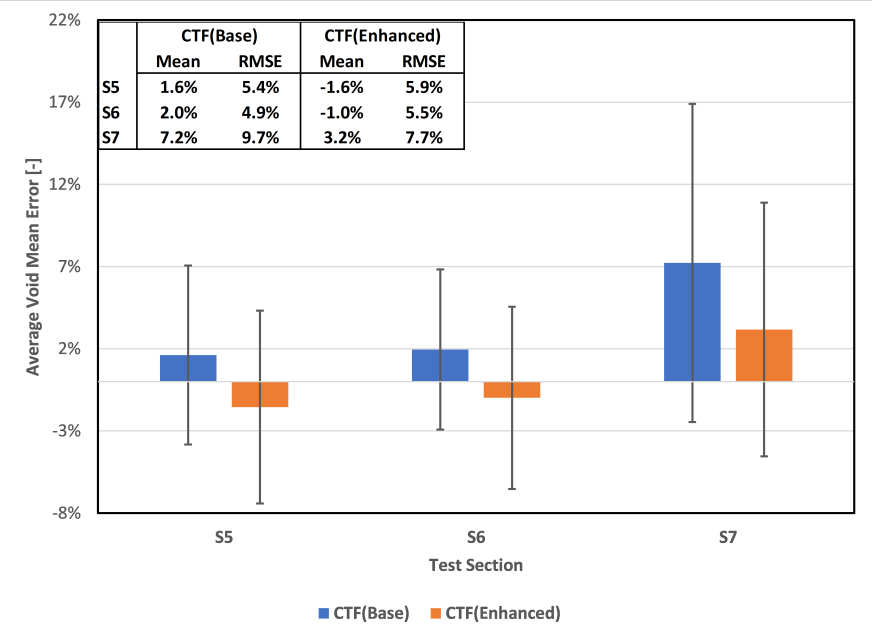

Figure 18. Mean error of void compared to experimental results for the three different series (S5, S6, S7) in the PSBT 5×5 bundle tests. Baseline models are shown in blue, and improved models (flow regime map, phase change, and wall heat transfer) are shown in orange. The standard deviation is shown with the uncertainty bars.

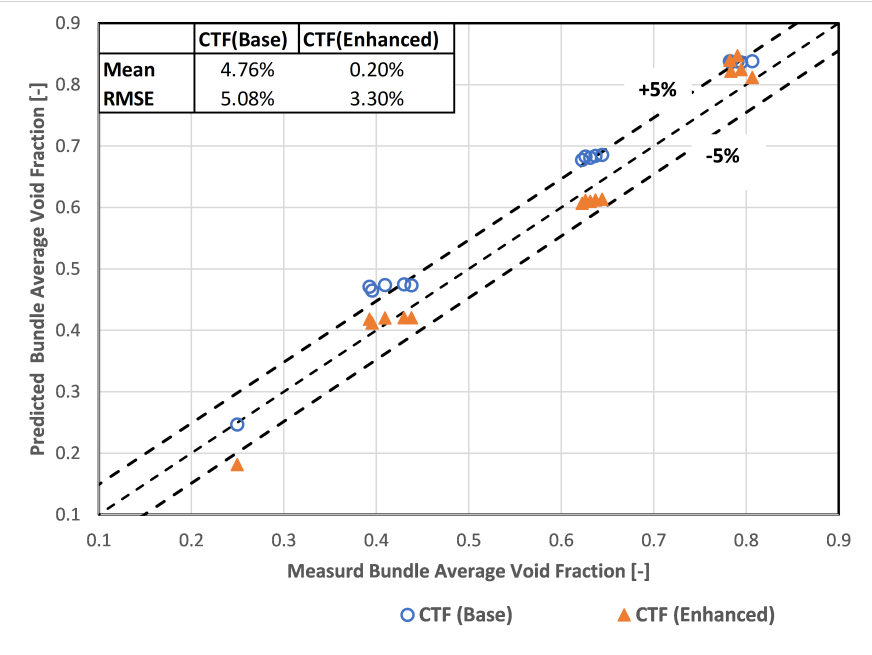

Figure 19. Comparison of CTF prediction of BFBT bundle tests with legacy and improved models (flow regime map, phase change, and wall heat transfer). Comparison is made for the bundle average void for each test series.

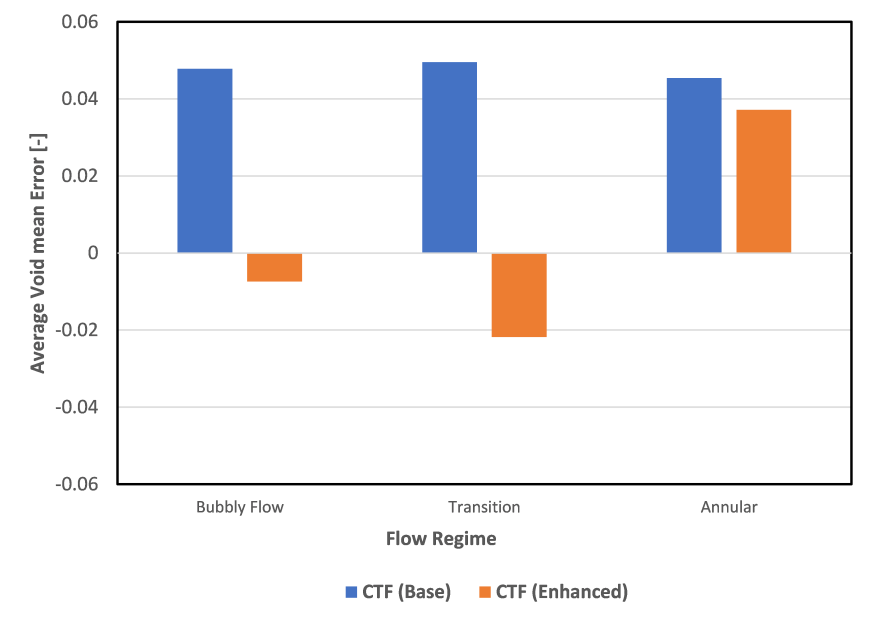

Figure 20. Mean void error between CTF and the BFBT bundle void data using legacy and improved models (flow regime map, phase change, and wall heat transfer). Experiments are organized based on the flow regime at the bundle outlet based on the mean outlet void.

trend is also consistent with that seen in the BFBT benchmark. A probable reason for this behavior is the linear interpolation of interfacial shear at the transition to annular flow, which is occurring at a much lower void than in CTF (Base). Additionally, comparisons of three selected tests results to axial void fraction are illustrated in Figs. 21b, 21c, and 21d. The controlling parameters for the calculation of void for those tests are essentially interfacial shear and the subcooled boiling model. The agreement between the measured and CTF (Enhanced) calculated results for the region below the transition to annular flow is excellent, but near the transition to annular flow region, the predicted voids are slightly lower than the measured ones.

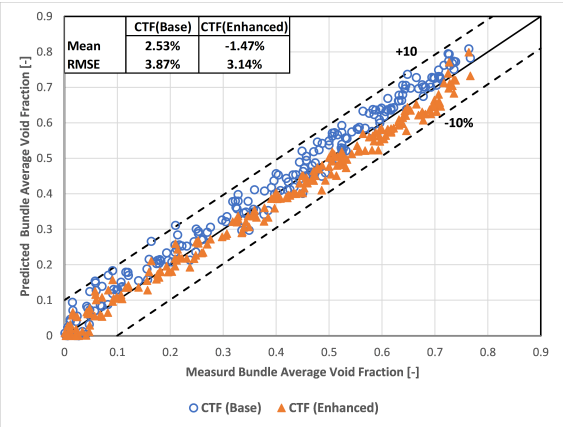

(a) Bundle average void.

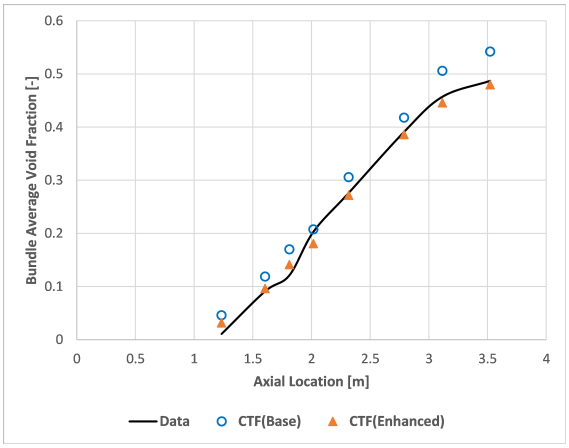

(b) Single axial void case 01.

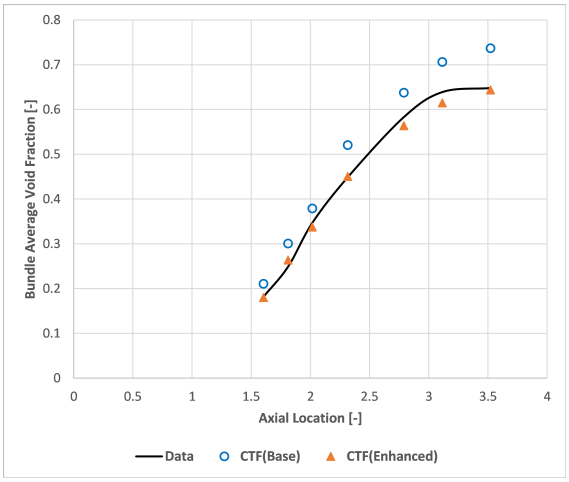

(c) Single axial void case 017.

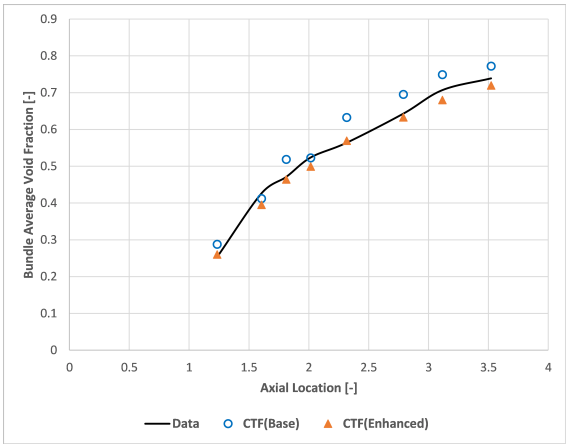

(d) Single axial void case 032.

Figure 21. FRIGG 713 axial bundle average void fraction comparison between CTF legacy models and improved models (flow regime map, phase change, and wall heat transfer).

3.5 ANNULAR MIST MODELS REVIEW

Annular gas-liquid flow is of considerable physical interest and has great practical significance. This flow is characterized by a thin liquid film adjacent to the wall and a high-speed gas core in the center of the flow. The gas-liquid interface, which separates the two continuous phases, is the route through which liquid is interchanged with droplet entrainment and re-deposition. As a crucial parameter, the entrainment of the droplets significantly alters the mechanisms of mass, momentum, and heat transfer between the liquid film and the gas core, as well as the transfer between the two-phase mixture and the wall. To accurately predict a number of important physical phenomena in annular-dispersed flow and in a post-dryout regime, an accurate correlation for the interfacial shear drag between droplet and vapor in the vapor core and between film and the vapor core is essential. The objective of this study is to review the interfacial shear at this flow regime and make recommendations to improve the code's void fraction prediction.

3.5.1 Droplet Interfacial Shear

When using the drift-velocity approach, the drag coefficient is formulated from a local steady-state force balance in the flow direction between buoyancy and interfacial drag forces for the gas and liquid phases in the core flow. The liquid and gas pressures are assumed to be equal. The interfacial drag per unit volume is then equal to the buoyancy force,

$$\tau'''_{i,ev} = \alpha_{v_c}(1 - \alpha_{v_c})g\Delta\rho, \tag{30}$$

where parameter g is the gravitational acceleration, $\Delta\rho$ is the liquid vapor density difference, α_{v_c} is the core vapor fraction, defined as

$$\alpha_{v_c} = \frac{\alpha_v}{\alpha_v + \alpha_e}, \tag{31}$$

and α_e and α_v are the droplet and vapor fractions, respectively, for the subchannel flow area. In dispersed flow, the drag force acting on the particle under steady-state conditions can be given in terms of the drag coefficient C_d, based on the relative velocity, as

$$\tau_{i,ev} = \frac{1}{2}C_d A_e \rho_v \left|\overline{V}_r\right| \overline{V}_r, \tag{32}$$

where A_e is the projected area for the drag on a single droplet, defined as $A_e = \frac{\pi d_e^2}{4}$. This force is related to the interfacial shear per unit volume for multiple particles, as

$$\tau'''_{i,ev} = \tau_{i,ev}\frac{\alpha_e}{V_e}, \tag{33}$$

where V_e is the volume of a single droplet given as $V_e = \frac{1}{6}\pi d_e^3$. Then, substituting Eq. (32) into Eq. (33) and replacing A_e and V_e by their expressions, the final form of the interfacial shear per unit volume is obtained:

$$\tau_{i,ev}^{'''} = \frac{3}{4}\frac{C_d}{d_e} < \alpha_e > \rho_g \left|\overline{V}_r\right| \overline{V}_r \tag{34}$$

$$\tau_{i,ev}^{'''} = \frac{3}{4}\frac{C_d}{d_e} < \alpha_e > \rho_g \left|\overline{V}_r\right| \overline{V}_r = \alpha_{v_c}(1 - \alpha_{v_c})g\Delta\rho. \tag{35}$$

The interfacial area per unit volume in dispersed droplet flow regime is defined as

$$A_i^{'''} = \frac{4A_p\alpha_e}{V_e} = \frac{6\alpha_e}{d_e}. \tag{36}$$

Using the definition of the interfacial area per unit volume from the expression in Eq. (36), Eq. (34) can be written in another popular form as

$$\tau_{i,ev}^{'''} = \frac{1}{8}C_d A_i^{'''} \rho_v \left|\overline{V}_r\right| \overline{V}_r. \tag{37}$$

In the drift flux approach, the drag on the droplet C_d is obtained by equating the interfacial drag expressed in Eq. (34) to the buoyancy given by Eq. (30). Thus,

$$C_d = \frac{4}{3}\frac{< \alpha_{vc} > \Delta\rho g d_e}{\rho_v \overline{V}_r^2}. \tag{38}$$

The relative velocity is related to the drift velocity by

$$\overline{V}_r = \frac{\overline{v}_{dj}}{1 - < \alpha_{vc} >}. \tag{39}$$

Substituting Eq. (39) into Eq. (38) leads to

$$C_d = \frac{4}{3}\frac{< \alpha_{vc} > (1 - < \alpha_{vc} >)^2 \Delta\rho g d_e}{\rho_v \overline{v_{dj}^2}}. \tag{40}$$

To convert the drift flux model into drag, the specification of the drift flux velocity (v_{dj}), the droplet diameter (d_e), and the distribution parameter C_0 are required. The average diameter is calculated from a critical Weber number (We_{crit}) of 12 and is given by:

$$d_e = \frac{\sigma We_{crit}}{\rho_v \overline{V}_r^2}, \tag{41}$$

and the drift flux velocity $\overline{v}_{dj}$ is correlated in the form of

$$\overline{v}_{dj} = k\,(1-\alpha_{vc})\left(\frac{\sigma\Delta\rho g}{\rho_v^2}\right)^{\frac{1}{4}}. \tag{42}$$

Substituting Eqs. (41) and (42) into Eq. (40) gives the form of the drag expression:

$$c_d = \frac{1}{k^4}\frac{4}{3}We_{crit}\alpha_{vc}. \tag{43}$$

Here, for calibration purposes, the k is introduced to the drift velocity, and its default value is $k = \sqrt{2}$. Using the drag expression Eq. (43) and the droplet diameter d_e from Eq. (41), Eq. (34) simplifies to

$$\tau'''_{i,ev} = \frac{1}{k^4}\frac{\alpha_{vc}\,(1-\alpha_{vc})}{\sigma}\rho_v^2\left|\overline{V}_r\right|^3\overline{V}_r. \tag{44}$$

According to Ishii's study on droplet size distribution and drag in annular flow (Ishii [1977]), the standard Weber number criteria based on the drift flux velocity in Eq. (41) can generate droplets that are far too large in comparison to droplets generated by high mass flux in the vapor core. This result has a significant implication in terms of the vapor superheating and post-dryout heat transfer. A number of small droplets have a large interfacial area between the liquid and vapor phases. Therefore, the amount of thermal non-equilibrium should not be very significant. In such cases, these small droplets act as a heat sink due to evaporation, so it tends to increase the post-dryout heat transfer. Thus, the particle radius may be approximated from the Weber-number criterion at the shearing-off of wave crests by employing the vapor core volumetric flux (J) instead of the relative velocity as

$$d_e = \frac{\sigma We_{crit}}{\rho_v J^2}. \tag{45}$$

The dispersed-flow drift velocity for the undistorted particle regime outside the stokes regime can be approximated by

$$V_{dj} = \frac{d_e}{4}\left[\frac{(g\Delta\rho)^2}{\mu_v\rho_v}\right]^{1/3}(1-\alpha_{vc})\,. \tag{46}$$

The above relations apply only when the total volumetric flux is sufficiently high to induce fragmentation of the wave crests. Hence, Eq. (46) should be used when

$$J > 1.456\left(\frac{\sigma g\Delta\rho}{\rho_v^2}\right)\left[\frac{\mu_v^2}{\rho_v\sigma\sqrt{\frac{\sigma}{g\Delta\rho}}}\right]^{-1/12}, \tag{47}$$

where J is the total volumetric flux given by

$$J = v_\ell\alpha_\ell + v_e\alpha_e + v_v\alpha_v. \tag{48}$$

The droplet drag is given by Eq. (40); substituting the drift velocity v_{dj} from Eq. (46) and the droplet diameter from Eq. (45), one can obtain an expression for $\frac{C_d}{d_e}$ of the form shown below:

$$\frac{C_d}{d_e} = \frac{16 \times \frac{4}{3}\rho_v J^4}{We_{crit}^2 \sigma^2} \frac{< \alpha_{vc} > \Delta\rho g}{\left[\frac{(g\Delta\rho)^2}{\mu_v \rho_v}\right]^{2/3}}. \tag{49}$$

Substituting the equation above into equation (34) leads to

$$\tau_{i,ev}''' = \frac{16}{We_{crit}^2} \frac{< \alpha_{vc} > (1 - < \alpha_{vc} >)\Delta\rho g \rho_v^2}{\sigma^2 \left[\frac{(g\Delta\rho)^2}{\mu_v \rho_v}\right]^{2/3}} J^4 \left|\overline{V}_r\right| \overline{V}_r. \tag{50}$$

In a recent study Ishii [2011], the previous expression that was provided for droplet diameter given by Eq. (45) was replaced by a more accurate expression:

$$d_e = 0.0099 \frac{\sigma}{\rho_v J_v^2} {Re_v}^{2/3} \left(\frac{\rho_v}{\rho_\ell}\right)^{-1/3} \left(\frac{\mu_v}{\mu_\ell}\right)^{2/3}. \tag{51}$$

The droplet drag is given by Eq. (40). By substituting the drift velocity v_{dj} from Eq. (46) and droplet diameter from Eq. (51), one can obtain an expression for $\frac{C_d}{d_e}$ of the form

$$\frac{C_d}{d_e} = \frac{4 \times 16}{3 \times 0.0099^2} \frac{< \alpha_{vc} > \Delta\rho g \rho_v}{\sigma^2 \left({Re_v}^{2/3} \left(\frac{\rho_v}{\rho_\ell}\right)^{-2/3} \left(\frac{\mu_v}{\mu_\ell}\right)^{2/3}\right)^2 \left[\frac{(g\Delta\rho)^2}{\mu_v \rho_v}\right]^{2/3}} J_v^4. \tag{52}$$

Substituting the equation above into Eq. (34) leads to

$$\tau_{i,ev}''' = \frac{16}{0.0099^2} \frac{< \alpha_{vc} > (1 - < \alpha_{vc} >)\Delta\rho g \rho_v^2}{\sigma^2 \left({Re_v}^{2/3} \left(\frac{\rho_v}{\rho_\ell}\right)^{-1/3} \left(\frac{\mu_v}{\mu_\ell}\right)^{2/3}\right)^2 \left[\frac{(g\Delta\rho)^2}{\mu_v \rho_v}\right]^{2/3}} J_v^4 \left|\overline{V}_r\right| \overline{V}_r, \tag{53}$$

where J_v is the vapor volumetric flux defined as $J_v = \alpha_v \rho_v v_v$, and Re_v is the vapor Reynolds number given by

$$Re_v = \frac{\alpha_v \rho_v v_v D_h}{\mu_v}. \tag{54}$$

In the derivation shown above, the droplet drag was derived from equating the drag force to the buoyancy. In another study (Ishii [1982]), Ishii showed that the viscous regime is very important for the droplet transport within the gas core flow. For this regime, Ishii gave an approximation to the drag coefficient in the following form:

$$C_d = \frac{10.67}{Re_e^{0.5}}, \tag{55}$$

where Re_e is the droplet Reynolds number, given as

$$Re_e = \frac{\rho_v \left|\overline{V}_r\right| d_e}{\mu_m}, \tag{56}$$

where μ_m is the mixture viscosity given by

$$\mu_m = \mu_v (1 - \alpha_{ec})^{-2.5}, \tag{57}$$

where α_{ec}) is the droplet core fraction given by $1 - \alpha_{vc}$). Based on Eq. (34), substituting the drag expression Eq. (55) and the droplet diameter from Eq. (45) leads to

$$\tau'''_{i,ev} = \frac{3 \times 10.67}{4 \times We_{crit}^{3/2}} \frac{(1 - < \alpha_{vc} >)\rho_v^2}{\sigma} \sqrt{\frac{\mu_m}{\sigma}} J^3 \left|\overline{V}_r\right|^{1/2} \overline{V}_r. \tag{58}$$

If the the droplet diameter from Eq. (51) is used instead, then the following expression is obtained for the interfacial shear:

$$\tau'''_{i,ev} = \frac{3 \times 10.67}{4 \times 0.0099^{3/2}} \frac{(1 - < \alpha_{vc} >)\rho_v^2}{\sigma} \sqrt{\frac{\mu_m}{\sigma}} \frac{1}{\left(Re_v^{2/3} \left(\frac{\rho_v}{\rho_\ell}\right)^{-1/3} \left(\frac{\mu_v}{\mu_\ell}\right)^{2/3}\right)^{3/2}} J_v^3 \left|\overline{V}_r\right|^{1/2} \overline{V}_r. \tag{59}$$

Ishii's work on drag coefficients on multi-particle systems for different flow regimes Mamoru Ishii [July 1982] are summarized in Fig. 22. As can be seen, the drag coefficient expressed by Eq. (55), which is provided in Ishii [1982] published by the same authors, was not included. Instead, Ishii reported a drag formulation at the viscous flow regime that is consistent with the formulation currently used by CTF:

$$C_d = 24 \frac{\left(1 + 0.1 Re_e^{0.75}\right)}{Re_e}. \tag{60}$$

With this drag and by using the droplet diameter from Eq. (45) one can derive an expression for the interfacial shear in the following form:

$$\tau'''_{i,ev} = \frac{3}{4 \times We_{crit}} \frac{24\left(1 + 0.1 Re_e^{0.75}\right)}{Re_e} \frac{(1 - < \alpha_{vc} >)\rho_v^2}{\sigma} J^2 \left|\overline{V}_r\right| \overline{V}_r, \tag{61}$$

where Re_e is the droplet Reynolds number defined by Eq. (56). The relation could be expanded to expose the relative velocity part for fully implicit discretization, but this would be complicated by the exponent (0.75) in the relationship, and it might not be beneficial enough to justify the effort. For simplicity, the Reynolds number can be evaluated at the previous time step.

When the droplet diameter is given by Eq. (51), the following expression can be derived for the interfacial shear:

$$\tau'''_{i,ev} = \frac{3}{4}\frac{24\left(1+0.1Re_e^{0.75}\right)}{Re_e}\frac{(1-<\alpha_{vc})\rho_v^2}{\sigma}\frac{J_v^2}{0.0099Re_v^{2/3}\left(\frac{\rho_v}{\rho_\ell}\right)^{-1/3}\left(\frac{\mu_v}{\mu_\ell}\right)^{2/3}}\left|\overline{V}_r\right|\overline{V}_r. \tag{62}$$

The relative velocity is defined as

$$\overline{V}_r = \frac{1-C_0<\alpha_{vc}>}{1-<\alpha_{vc}>}\overline{v}_g - C_0\overline{v}_e, \tag{63}$$

Where C_0 is the distribution parameter and is assumed (according to Ishii) to be proportional to the density ratio (ρ_v/ρ_ℓ) and the Reynolds number based on saturated liquid properties in the following form,

$$C_0 = C_\infty - (C_\infty - 1)\sqrt{\rho_v/\rho_\ell} \tag{64}$$

. The C_∞ is given by

$$C_\infty = 1.399 - 0.0155ln(Re_\ell). \tag{65}$$

In summary, the above derivation of interfacial shear can be combined in six options, depending on whether the the drag is explicit or if it is based on buoyancy, and what expression is used for the droplet diameter size. This is summarized graphically in Fig.23−24 and is explicitly reflected in Eqs. (66) through (71).

Option 1:

$$\tau'''_{i,ev} = \begin{cases} \frac{1}{k^4}\frac{\alpha_{vc}(1-\alpha_{vc})}{\sigma}\rho_v^2\left|\overline{V}_r\right|^3\overline{V}_r & \text{if } J \le 1.456\left(\frac{\sigma g\Delta\rho}{\rho_v}\right)\left[\frac{\mu_v^2}{\rho_v\sigma\sqrt{\frac{\sigma}{g\Delta\rho}}}\right]^{-1/12} \\ \frac{16}{We_{crit}^2}\frac{<\alpha_{vc}>(1-<\alpha_{vc}>)\Delta\rho g\rho_v^2}{\sigma^2\left[\frac{(g\Delta\rho)^2}{\mu_v\rho_v}\right]^{2/3}}J^4\left|\overline{V}_r\right|\overline{V}_r & \text{if } J > 1.456\left(\frac{\sigma g\Delta\rho}{\rho_v}\right)\left[\frac{\mu_v^2}{\rho_v\sigma\sqrt{\frac{\sigma}{g\Delta\rho}}}\right]^{-1/12} \end{cases} \tag{66}$$

Option 2:

$$\tau'''_{i,ev} = \begin{cases} \frac{1}{k^4}\frac{\alpha_{vc}(1-\alpha_{vc})}{\sigma}\rho_v^2\left|\overline{V}_r\right|^3\overline{V}_r & \text{if } J \le 1.456\left(\frac{\sigma g\Delta\rho}{\rho_v}\right)\left[\frac{\mu_v^2}{\rho_v\sigma\sqrt{\frac{\sigma}{g\Delta\rho}}}\right]^{-1/12} \\ \frac{16}{0.0099^2}\frac{<\alpha_{vc}>(1-<\alpha_{vc}>)\Delta\rho g\rho_v^2}{\sigma^2\left(Re_v{}^{2/3}\left(\frac{\rho_v}{\rho_\ell}\right)^{-1/3}\left(\frac{\mu_v}{\mu_\ell}\right)^{2/3}\right)^2\left[\frac{(g\Delta\rho)^2}{\mu_v\rho_v}\right]^{2/3}}J_v^4\left|\overline{V}_r\right|\overline{V}_r & \text{if } J > 1.456\left(\frac{\sigma g\Delta\rho}{\rho_v}\right)\left[\frac{\mu_v^2}{\rho_v\sigma\sqrt{\frac{\sigma}{g\Delta\rho}}}\right]^{-1/12} \end{cases} \tag{67}$$

Option 3:

$$\tau'''_{i,ev} = \begin{cases} \frac{1}{k^4}\frac{\alpha_{vc}(1-\alpha_{vc})}{\sigma}\rho_v^2\left|\overline{V}_r\right|^3\overline{V}_r & \text{if } J \le 1.456\left(\frac{\sigma g\Delta\rho}{\rho_v}\right)\left[\frac{\mu_v^2}{\rho_v\sigma\sqrt{\frac{\sigma}{g\Delta\rho}}}\right]^{-1/12} \\ \frac{3\times10.67}{4\times We_{crit}^{3/2}}\frac{(1-<\alpha_{vc}>)\rho_v^2}{\sigma}\sqrt{\frac{\mu_m}{\sigma}}J^3\left|\overline{V}_r\right|^{1/2}\overline{V}_r & \text{if } J > 1.456\left(\frac{\sigma g\Delta\rho}{\rho_v}\right)\left[\frac{\mu_v^2}{\rho_v\sigma\sqrt{\frac{\sigma}{g\Delta\rho}}}\right]^{-1/12} \end{cases} \tag{68}$$

Option 4:

$$\tau_{i,ev}^{'''} = \begin{cases} \frac{1}{k^4}\frac{\alpha_{vc}(1-\alpha_{vc})}{\sigma}\rho_v^2\left|\overline{V}_r\right|^3\overline{V}_r & \text{if } J \le 1.456\left(\frac{\sigma g\Delta\rho}{\rho_v}\right)\left[\frac{\mu_v^2}{\rho_v\sigma\sqrt{\frac{\sigma}{g\Delta\rho}}}\right]^{-1/12} \\ \frac{3\times 10.67}{4\times 0.0099^{3/2}}\frac{(1-<\alpha_{vc}>)\rho_v^2}{\sigma}\sqrt{\frac{\mu_m}{\sigma}}\frac{1}{\left(Re_v^{2/3}\left(\frac{\rho_v}{\rho_\ell}\right)^{-1/3}\left(\frac{\mu_v}{\mu_\ell}\right)^{2/3}\right)^{3/2}} & \\ J_v^3\left|\overline{V}_r\right|^{1/2}\overline{V}_r & \text{if } J > 1.456\left(\frac{\sigma g\Delta\rho}{\rho_v}\right)\left[\frac{\mu_v^2}{\rho_v\sigma\sqrt{\frac{\sigma}{g\Delta\rho}}}\right]^{-1/12} \end{cases} \quad (69)$$

Option 5:

$$\tau_{i,ev}^{'''} = \begin{cases} \frac{1}{k^4}\frac{\alpha_{vc}(1-\alpha_{vc})}{\sigma}\rho_v^2\left|\overline{V}_r\right|^3\overline{V}_r & \text{if } J \le 1.456\left(\frac{\sigma g\Delta\rho}{\rho_v}\right)\left[\frac{\mu_v^2}{\rho_v\sigma\sqrt{\frac{\sigma}{g\Delta\rho}}}\right]^{-1/12} \\ \frac{3}{4\times We_{crit}}\frac{24\left(1+0.1Re_e^{0.75}\right)}{Re_e}\frac{(1-<\alpha_{vc}>)\rho_v^2}{\sigma}J^2\left|\overline{V}_r\right|\overline{V}_r & \text{if } J > 1.456\left(\frac{\sigma g\Delta\rho}{\rho_v}\right)\left[\frac{\mu_v^2}{\rho_v\sigma\sqrt{\frac{\sigma}{g\Delta\rho}}}\right]^{-1/12} \end{cases} \quad (70)$$

Option 6:

$$\tau_{i,ev}^{'''} = \begin{cases} \frac{1}{k^4}\frac{\alpha_{vc}(1-\alpha_{vc})}{\sigma}\rho_v^2\left|\overline{V}_r\right|^3\overline{V}_r & \text{if } J \le 1.456\left(\frac{\sigma g\Delta\rho}{\rho_v}\right)\left[\frac{\mu_v^2}{\rho_v\sigma\sqrt{\frac{\sigma}{g\Delta\rho}}}\right]^{-1/12} \\ \frac{3}{4}\frac{24\left(1+0.1Re_e^{0.75}\right)}{Re_e}\frac{(1-<\alpha_{vc}>)\rho_v^2}{\sigma}\frac{J_v^2}{0.0099Re_v^{2/3}\left(\frac{\rho_v}{\rho_\ell}\right)^{-1/3}\left(\frac{\mu_v}{\mu_\ell}\right)^{2/3}}\left|\overline{V}_r\right|\overline{V}_r & \text{if } J > 1.456\left(\frac{\sigma g\Delta\rho}{\rho_v}\right)\left[\frac{\mu_v^2}{\rho_v\sigma\sqrt{\frac{\sigma}{g\Delta\rho}}}\right]^{-1/12} \end{cases} \quad (71)$$

	Fluid Particle System			Solid Particle System
	Bubble in Liquid	Drop in Liquid	Drop in Gas	
Viscosity Model	$\frac{\mu_m}{\mu_c} = \left(1 - \frac{\alpha_d}{\alpha_{dm}}\right)^{-2.5\alpha_{dm}\mu^*}$, $\mu^* \equiv \frac{\mu_d + 0.4\mu_c}{\mu_d + \mu_c}$			
Max. Packing α_{dm}	~ 1	~ 1	$0.62 \sim 1$	~ 0.62
μ^*	0.4	~ 0.7	1	1
μ_m/μ_c	$(1-\alpha_d)^{-1}$	$(1-\alpha_d)^{-1.75}$	$\sim (1-\alpha_d)^{-2.5}$	$\left(1 - \frac{\alpha_d}{0.62}\right)^{-1.55}$
Stokes Regime C_D	$C_D = \frac{24}{N_{Re}}$ where $N_{Re} \equiv \frac{2r_d\rho_c v_r}{\mu_m}$			
Viscous Regime C_D	$C_D = \frac{24\left(1 + 0.1N_{Re}^{0.75}\right)}{N_{Re}}$			
Newton's Regime C_D	———			$C_D = 0.45\left[\frac{1+17.67\left\{f(\alpha_d)\right\}^{6/7}}{18.67 f(\alpha_d)}\right]^2$ where $f(\alpha_d) = \sqrt{1-\alpha_d}\left(\frac{\mu_c}{\mu_m}\right)$
Distorted Particle Regime C_D	$C_D = \frac{4}{3} r_d \sqrt{\frac{g\Delta\rho}{\sigma}}\left[\frac{1+17.67\left\{f(\alpha_d)\right\}^{6/7}}{18.67 f(\alpha_d)}\right]^2$ $f(\alpha_d) = (1-\alpha_d)^{1.5} \quad (1-\alpha_d)^{2.25} \quad (1-\alpha_d)^3$			
Churn-turbulent Flow Regime C_D	$C_D = \frac{8}{3}(1-\alpha_d)^2$			
Slug Flow C_D	$C_D = 9.8(1-\alpha_d)^3$			

Figure 22. Ishii and Chawla: Local drag coefficients in multiparticle system.

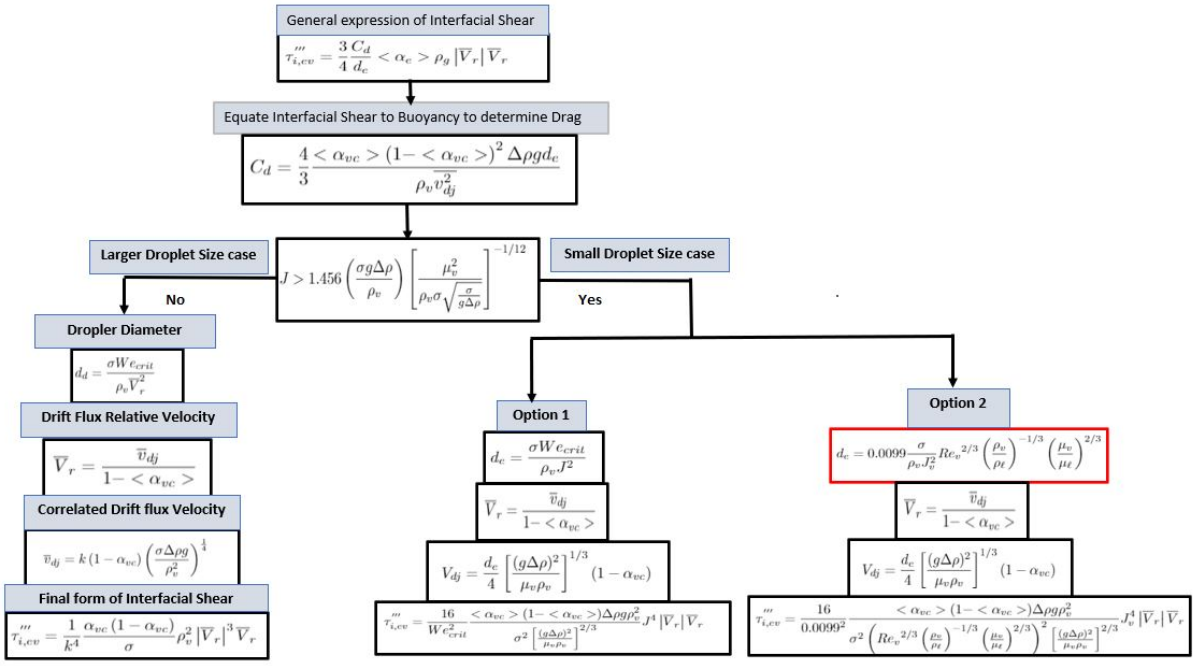

Figure 23. Droplet interfacial shear based on buoyancy approach.

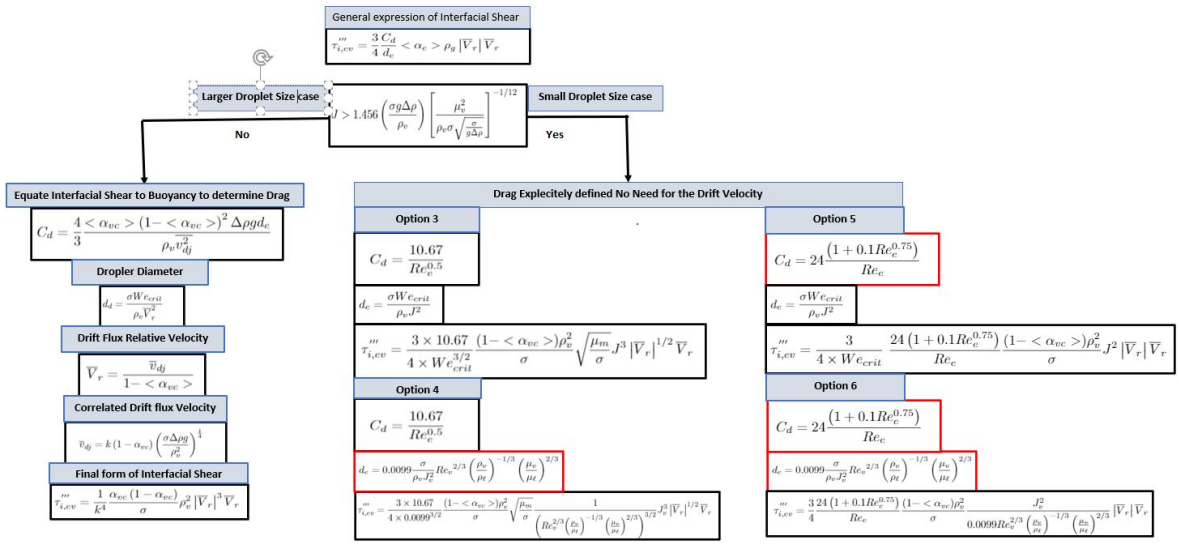

Figure 24. Droplet interfacial shear based on explicit drag.

3.5.2 Interfacial Shear Film to Vapor Core

The film interfacial shear was previously reviewed in Salko et al. [2020b]. For the sake of completeness, the findings of that review are briefly repeated here. The interfacial shear can be approximated according to Wallis [1969] as

$$\tau_{i,fc}^{'''} = \frac{1}{2} f_i A_i^{'''} \rho_v \left|\overline{V}_r\right| \overline{V}_r, \tag{72}$$

where $A_i^{'''}$ is the interfacial area per unit volume, given as

$$A_i^{'''} = \frac{4\sqrt{\alpha_v + \alpha_e}}{D_h}, \tag{73}$$

and f_i is the friction factor which is calculated by two approaches, depending on whether the film is stable or unstable. For stable film, this is given by the Wallis correlation:

$$f_i = 0.005(1 + 75\alpha_\ell). \tag{74}$$

For unstable film, CTF used the Henstock and Hanratty correlation; however, this model has been questioned, as it contributes dramatically to overprediction of the pressure drop, as was shown in Salko et al. [2020b] recent test results. The recommendation was to remove it and use only the friction factor based on stable film. This recommendation is being utilized when the new flow regime map (discussed in Section 3.4) is enabled. As stated in Section 3.4, CTF tends to overpredict the void fraction in annular flow due the high magnitude of the interracial shear that is applied to the vapor. One way to improve this overprediction is to reduce the interfacial shear applied to the vapor. Section 3.5.1 discusses the use of the drift flux approach for this purpose. The other approach is to split the film/core interfacial shear between droplet and vapor proportional to their fraction, as shown in Eq.(75). Qualification of data will determine whether the two approaches should be combined, or if only one of them will be used.

3.5.3 Interfacial Shear Work Progress Summary

The mathematical detail of the interfacial shear in the core and between the film and the vapor core was discussed. The work progress for those tasks can be summarized as follows:

- For the core's interfacial shear between droplet and vapor, six options have been developed based on drift flux. All of the options are implemented into the code, and the only remaining work is to compare the results to experimental data to determine which option best matches the data.
- An additional modification to the film/core interfacial drag is being proposed to further reduce the interfacial shear acting on the vapor. In this approach, instead of fully applying the film/core interfacial shear to the vapor, it will be divided between droplet and vapor, proportional to their fraction. This task has not been implemented yet, but the approach is summarized as follows:

$$\begin{aligned} \tau_{i,fv}''' &= \tau_{i,fc}''' \frac{\alpha_v}{\alpha_v + \alpha_e} \\ \tau_{i,fe}''' &= \tau_{i,fc}''' \frac{\alpha_e}{\alpha_v + \alpha_e} \end{aligned}, \tag{75}$$

where $\tau_{i,fv}'''$ is the interfacial shear between film and vapor, $\tau_{i,fe}$ is the interfacial shear between film and droplet, and $\tau_{i,fc}'''$ is the interfacial shear between film and core.

4. CLOSURE MODEL CALIBRATION

4.1 BACKGROUND

While the previous sections discuss implementation of newer models that will be more accurate than the existing legacy models in CTF, those models often have uncertain modeling parameters that are limited to the original data, or assumptions that were used to set their values. Therefore, a process was undertaken to recalibrate these modeling parameters using data analytic tools and new experimental data. The calibration work expands on the milestone report that was released last year (Salko et al. [2020b]). The approach, which is described in detail in the aforementioned report, uses Bayesian inference to calibration problems, as it provides both the optimal parameter values and the uncertainty associated with each free parameter given the experimental data. To summarize the Bayesian Inference approach, let the model predictions be denoted by $y_m|_{\boldsymbol{\theta}}$, where $\boldsymbol{\theta}$ represents a set of model parameters, such as the unknown leading coefficients in a closure model. Assuming the residual, which is defined as the difference between the model predictions and the experimental data, $r_i = y_m|_{\boldsymbol{\theta}} - y_{i,d}$, follows a Gaussian-like distribution, $r \sim \mathcal{N}(0, \theta_\sigma)$, with unknown standard deviation θ_σ. The goal is to find the probability density of $\boldsymbol{\theta}$, given the data, $\pi(\boldsymbol{\theta}|y_d)$. This is also known as the *posterior probability density function (PDF)* and is given by

$$\pi(\boldsymbol{\theta}|y_d) = \frac{\pi(y_d|\boldsymbol{\theta})p(\boldsymbol{\theta})}{\int \pi(y_d|\boldsymbol{\theta})p(\boldsymbol{\theta})d\boldsymbol{\theta}}, \tag{76}$$

where the likelihood function, $\pi(y_d|\boldsymbol{\theta})$, is defined as follows:

$$\pi(y_d|\boldsymbol{\theta}) = \frac{1}{\left(2\pi\theta_\sigma^2\right)^{N/2}} exp\left(-\frac{SSE}{2\theta_\sigma^2}\right). \tag{77}$$

The prior distribution, $p(\boldsymbol{\theta})$, is a free choice in the Bayesian approach. In principle, the prior can be any valid density function, and for the calibration study, flat, uniform priors were used.

A numerical approach employing Markov-chain Monte Carlo (MCMC) is used to circumvent the computation of the integral in the denominator of Eq. (76). The Differential Evolution Adaptive Metropolis (DREAM) MCMC algorithm is used to draw samples from Eq. (76). DREAM was selected because it is robust to multimodal distributions, automatically adapts to the scale of the posterior without having to specify parameters governing a proposal distribution, and is easily run in parallel. BiPyMc is a Python package (Gurecky [2018]) developed to solve general inference problems, including model calibration problems. BiPyMc implements the DREAM MCMC algorithm Vrugt et al. [2008] and other adaptive differential evolution-based MCMC algorithms. BiPyMc also has the capability to generate surrogates using Gaussian process regression and is the method of choice to train surrogates in the current study. Additional details on the MCMC algorithm used in the current study are available in Salko et al. [2020b].

4.2 PREVIOUS CALIBRATION STUDY

In the previous study, the default CTF models for the wall drag and interfacial drag were exposed and calibrated with experimental data. The disadvantage of this approach is that by definition, these multipliers

are single point values which might not be applicable for varying flow conditions and flow geometries. However, these multipliers serve as starting points to demonstrate the approach and could be extended to calibration of physical parameters that are independent of flow condition and geometry. Initially, six multipliers were chosen, including a multiplier for the nucleate boiling heat transfer coefficient, which was later dropped because of low sensitivity. The definitions of the final five chosen multipliers are given in Table 5.

Table 5. Chosen calibration parameters

Multiplier	Description	Default
k_xkwlxA	Two-phase wall drag coefficient A in $\Phi^2 = A\alpha_l^B$	1.0
k_xkwlxB	Two-phase wall drag coefficient B in $\Phi^2 = A\alpha_l^B$	-2.0
k_xk_sb	Small bubble interfacial drag coefficient multiplier	1.0
k_xk_slg	Slug bubble interfacial drag coefficient multiplier	1.0
k_xk_anrflm	Annular-mist liquid film interfacial drag coefficient multiplier	1.0

Experimental datasets with void fraction and two-phase pressure-drop measurements were selected for calibration. The PSBT single-channel tests were chosen to calibrate the interfacial drag coefficients in the small bubble and slug flow regimes, because the majority of the tests span those two flow regimes. On the other hand, the BFBT (Assembly Type 1) and Risø 200 series (unheated tests) tests were expected to be critical for influencing the optimum value for the annular liquid film drag multiplier and two-phase multiplier parameters. The bounds for the five multipliers were selected after gauging the response from a sensitivity analysis, which was conducted independently for each of the five multipliers.

Because of the computational expense in running CTF for each set of multipliers for an MCMC evaluation, a surrogate model was developed to mimic the chosen CTF response to independent model parameters and boundary conditions. The Gradient boosting technique was chosen because of its ease of training and its fast training times for large data sets. The disadvantage with the Gradient boosting technique is its piece-wise constant surface prediction, which may not result in smooth posterior distributions.

Once the surrogates were trained for the three datasets, the DREAM-based calibration was performed by using 10 chains executed for 20,000 generations, resulting in a total of 200,000 samples. The first 2,000 generations were discarded as burn-in generations to allow the chains to properly mix to converge to a stationary PDF. The calibration results showed that for each of the five parameters, the chains do not mix well with the increasing number of samples and stay at a constant value. Furthermore, the pair-wise distributions were not smooth, and they had clustered samples. This indicated that for this application, alternative machine learning tools such as the Gaussian process regression and support vector machines were more appropriate.

The median values for the interfacial and wall drag multipliers were significantly less than their base value, indicating the over-prediction of interfacial drag, which causes over-prediction of void fraction and two-phase pressure drop. The validation matrix in CTF was re-run with the median-calibrated multipliers. The impact of the multipliers can be separated into two categories: calibrated and non-calibrated datasets. Generally, the calibrated model resulted in improved void fraction predictions for the tests used for calibration: the PSBT single-channel tests and the BFBT bundle tests. The impacts of the multipliers for tests that were not part of the calibration process, such as the PSBT bundle tests, were more modest. This demonstrated the deficiencies of the method with regards to the selected multipliers. Overall, it was

observed that transitioning to the drift flux model, for example, could result in improved void predictions because the model lends itself to more physically appropriate tuning coefficients.

The maximum improvement in the two-phase pressure-drop prediction was obtained for the Risø tests. This was observed to be largely driven by the low optimum wall drag multipliers and improved void fraction predictions in the annular flow regime via the liquid film interfacial drag multiplier. Finally, the calibrated model predictions for the wall temperature were largely unchanged from the base model predictions. This is expected since these are driven by the wall heat transfer model. It was observed that further improvements to the wall heat transfer model were required to improve the wall temperature predictions.

4.3 SENSITIVITY ANALYSES FOR THE CHISHOLM MODEL

In the current study, a new set of model parameters and multipliers is selected for calibration. The difference between closure model parameters and multipliers is that model parameters are used for tuning specific coefficients in the closure model, such as an exponent of a non-dimensional parameter, whereas a multiplier is a simple constant coefficient to the whole model. Therefore, model parameters could be applicable for a range of flow conditions. The Chisholm wall drag model, which is described in Section 3.1, is initially exposed to six parameters. The six exposed Chisholm parameters are chosen in the following manner: k_xkwlxChA is used to calibrate the effect of the slip ratio (Eq. 9), k_xkwlxChB is used to calibrate the effect of the ratio of friction factors (Eq. 5), k_xkwlxChC is a simple additive parameter, k_xkwlxChE and k_xkwlxChF are jointly used to calibrate the effect of 'B' (Eq. 8) with mass flux, and k_xkwlxChG is used to calibrate the the change of the two-phase multiplier with quality (Eq. 7). The parameters (abbreviated) are defined starting with Eq. 8 as follows:

$$B_{calib} = \frac{C^{ChA}\Gamma^{ChB} - ChC}{\left(ChE + \frac{Re_l}{ChF}\right)\left(\Gamma^2 - 1\right)}, \tag{78}$$

Where Re_l is a liquid only Reynolds number, calculated using the total mass flux. Substituting B_{calib} into Eq. (7), we obtain:

$$\Phi^2_{lo,calib} = 1 + \left(\Gamma^2 - 1\right)\left(B_{calib} x_{\text{flow}}\left(1 - x_{\text{flow}}\right) + x^{ChG}_{\text{flow}}\right). \tag{79}$$

It must be noted that Eq. (79) is consistent with the limiting cases of single-phase liquid and single-phase vapor. The base value of the six parameters are as follows:

Table 6 also shows the preliminary ranges of the exposed parameters which were determined through initial sensitivity studies. As a first step, Dakota was used to perform a sensitivity analysis of select Risø 500 series (adiabatic) tests to determine the ranges of the six parameters. Before performing the sensitivity analysis, k_xkwlxChB and k_xkwlxChC were fixed in-order to reduce the dimensionality of the surrogate model that would be required for calibration. While k_xkwlxChC is fixed to its base value, k_xkwlxChB is fixed to 2.0 (default value of 1.0). This was determined by calibrating the Chisholm model independently with k_xkwlxChB. Therefore, the Dakota study was performed with the four parameters: k_xkwlxChA, k_xkwlxChE, k_xkwlxChF, and k_xkwlxChG. In order to run CTF-Dakota, integration of these parameters with Workbench (Lefebvre et al. [2019]) is accomplished via the Subchannel Modeling and Analysis Toolkit (SubKit) front-end tool for CTF. Additionally, drift flux model parameters were also exposed

Table 6. Exposed Chisholm parameters

Multiplier	Default	Prelim. ranges
k_xkwlxChA	1.0	0.2-2.0
k_xkwlxChB	1.0	1.0-2.5
k_xkwlxChC	2.0	0.2-2.5
k_xkwlxChE	1.0	0.2-2.0
k_xkwlxChF	1.e10	1.e3-1.e6
k_xkwlxChG	2.0	0.2-2.5

before the sensitivity analysis was performed. Including these parameters demonstrates that the quality-based Chisholm model is insensitive to interfacial drag parameters, unlike the base Wallis model, which is more strongly coupled to the interfacial drag model. For the purpose of the analysis, the exposed drift flux parameters are defined here for the distribution parameter $C_{0,bc}$ (Eq. 18) and for the constant k in the drift velocity $\overline{V}_{gj,bc}$ (Eq. 19) as:

$$C_{0,calib} = k\_C_0 \left(C_{\infty,bc} - (C_{\infty,bc} - 1) \sqrt{\frac{\rho_v}{\rho_\ell}} \right) \tag{80}$$

$$\overline{V}_{gj,calib} = k\_kcoeff \left(k \left(\frac{\sigma \Delta \rho g}{\rho_\ell^2} \right)^{\frac{1}{4}} \right). \tag{81}$$

The multiplier for k in Eq.)81) is dependent on the flow regime and is expressed as k_kcoeff_sb for small bubble, and k_kcoeff_slg for cap/slug bubble. The last parameter included in the sensitivity analysis is the multiplier to the liquid film in the annular-mist flow regime, defined in Table 5. The CTF-Dakota sensitivity analysis was performed for a total of 400 samples (50 per multiplier), with the residual vector defined as the difference between the experimental and CTF two-phase pressure drop values for 8 select Risø 500 series tests. The results of the analysis are shown in Fig. (25) in terms of the absolute partial rank correlation for the eight conditions against seven of the eight multipliers. The seven multipliers are abbreviated in the legend for compactness, with *SB* representing k_kcoeff_sb, *Anrflm* representing k_xk_anrflm, and the four Chisholm parameters as defined in Eq. (78).

Based on results from the sensitivity analysis, it can be observed that the four Chisholm parameters are overwhelmingly the most sensitive parameters and are calibrated using Bayesian inference.

4.4 DEVELOPMENT OF SURROGATES

Gaussian processes are a generalized, supervised machine learning method applicable to both regression and classification problems. A Gaussian process is a collection of random variables, any finite number of which have a joint (multivariate) Gaussian distribution (Rasmussen and Williams [2006]) and can be expressed as

$$f(x) \sim GP\left(m(x), k(x, x')\right)., \tag{82}$$

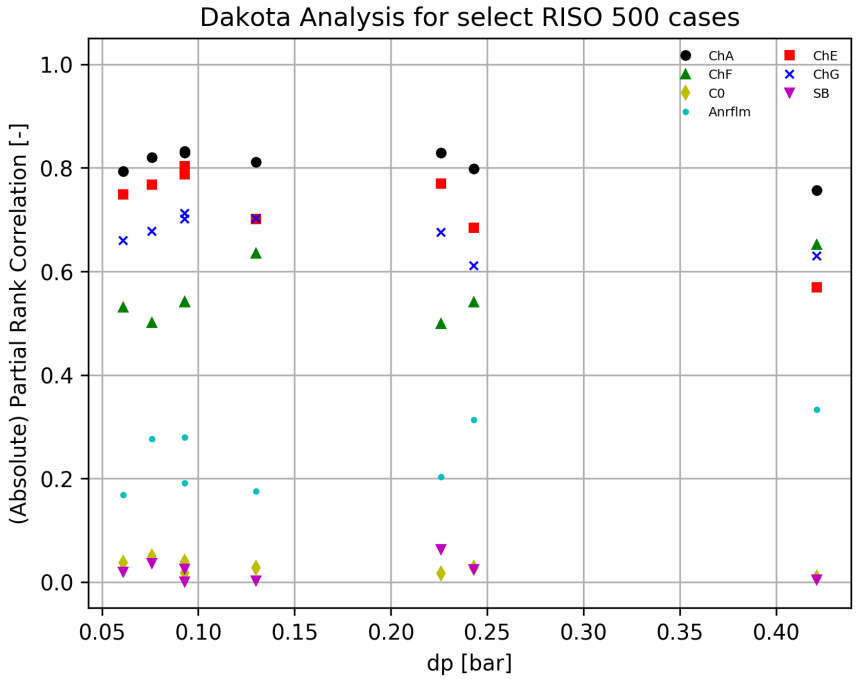

Figure 25. Result of the CTF-Dakota sensitivity analysis for eight select Risø 500 series cases.

where $m(x)$ is the mean function, which is usually taken to be zero, and $k(x, x')$ is the covariance function. Using a Bayesian approach, the posterior distribution can be determined from a Gaussian process (GP) prior and conditioned on the experimental observations (training data). The joint distribution of the training outputs, f, and the test outputs, f_*, according to the prior, is as follows (Rasmussen and Williams [2006]):

$$f_*|X_*, X, f \sim N\left(K\left(X_*, X\right) K\left(X, X\right)^{-1} f, K\left(X_*, X_*\right) - K\left(X_*, X\right) K\left(X, X\right)^{-1} K\left(X, X_*\right)\right), \tag{83}$$

where for n training points and n_* test points, $K\left(X, X_*\right)$ denotes the $n \times n_*$ matrix of covariances evaluated at all pairs of training and test points, $K\left(X, X\right)$ denotes the $n \times n$ matrix of covariances evaluated at all pairs of training points, and so on. The mean of the distribution from Eq. (83) is the prediction at the n_* test points, and the covariance is the predictive variance. A practical implementation of GP regression uses Cholesky decomposition to invert the covariance matrix (Rasmussen and Williams [2006]). The primary advantage of using GP regression is that it can not only return the mean of the prediction, but it can also provide the variance and the marginal likelihood function. Secondly, the PDF is a smooth function unlike the piece-wise constant surface prediction returned by the gradient boosting method, so is more likely to return smoother output functions for calibration using Bayesian inference. The main drawback of this approach is that although GP regression works very well for small training data set sizes, the running time which scales as $\sim O(n^3)$, where n is the size of the training dataset, becomes prohibitively expensive for large datasets. The GP regression implementation in BiPyMc used in the current study is based on Rasmussen and Williams [2006]. The squared exponential kernel parameters in BiPyMc were optimized using the DIRECT algorithm Finkel [2005]. The selected GP regression hyperparameters are summarized in Table 7. Future work may include tuning the model hyperparameters, perhaps using MCMC, improving the model's ability to generalize to previously unseen data.

Table 7. Hyperparameters for the GP regression

Parameter name	Value or type
Kernel	Squared exponential
Optimization algorithm	modified direct algorithm
Approximate upper bound on likelihood function evaluations	600

The surrogate model, which is developed for the Risø dataset in the current study, departs from the earlier approach of using fixed boundary conditions for series 200. The primary reason for not restricting the model to series 200 is that the hydraulic diameter of the flow geometry is not taken into account in the surrogate model. As in the previous study, the heated cases are ignored to isolate the effect of the wall drag (frictional) model on the pressure drop. The heated cases have a large contribution from buoyancy and a non-negligible contribution of the acceleration pressure drop. The wall drag pressure drop is inversely proportional to the hydraulic diameter and is therefore taken to be a model parameter in the current study. To generate a training dataset to accommodate all the Risø adiabatic series (200, 500, 600), the fixed boundary condition approach is discarded in favor of "synthetic" boundary conditions, meaning that the boundary conditions selected do not necessarily match those of the experiments themselves. Because the synthetic boundary conditions are essentially independent model parameters, the surrogate developed from the training data is better correlated to the range of boundary conditions, which is not the case when using fixed boundary conditions. It must be noted that when using the surrogate for calibration, actual experimental bcs are used. The hydraulic diameter is fixed to 9 mm, 10 mm, and 20 mm (for series 500, 200, and 600, respectively) for each set of training/testing data conditions, which include both boundary conditions and the four Chisholm parameters. The final ranges of the eight model parameters are as follows:

Table 8. Bounds of model parameters to generate training/testing data for the Risø surrogate

Model parameter	Ranges
system pressure (bar)	30–90
mass flux ($kg/m^2 - s$)	400–3000
exit quality (-)	$3{\cdot}10^{-4}$–0.90
hydraulic diameter (mm)	9,10,20
k_xkwlxChA (-)	0.2–2.0
k_xkwlxChE (-)	0.2–2.0
k_xkwlxChF (-)	$1{\cdot}10^{3}$–$1{\cdot}10^{6}$
k_xkwlxChG (-)	0.5–2.5

The Latin hypercube sampling method Bouhlel et al. [2019] was used to generate random samples for the seven varying model parameters for three hydraulic diameters. While generating the training/testing data, both k_xkwlxChB and k_xkwlxChC were fixed at 2.0. A key reason for fixing k_xkwlxChB is that the quality of the surrogate was poor when it was jointly trained along with the other four Chisholm model parameters. The number of training/testing datasets was varied, keeping in mind the increase in computational cost for a large number of points. The prediction of the surrogate vs. testing data which was developed with 5,698 (converged) training points and tested with 5,698 (converged) testing points, is

shown in Fig. 26 against three model parameters. Although the quality of the surrogate is not as good as those obtained from the previous study using gradient boosting, it is deemed to be acceptable with a RMSE of $3.5{\cdot}10^{-2}$ bar.

4.5 CALIBRATION

As in the previous study, the DREAM-based calibration was performed on the trained surrogate by using 10 chains executed for 10,000 generations, resulting in a total of 100,000 samples. The first 2,000 generations were discarded as burn-in generations, allowing the chains to properly mix in order to converge to a stationary PDF. Experimental data corresponding to Series 200, 500, and 600 were used to calculate the residual vector for calibration. Additionally, to avoid over-fitting by calibrating with all the available experimental data, the overall dataset was divided into training and testing datasets using the k-fold cross-validation tool in sci-kit learn Pedregosa et al. [2011]. Five folds were used to split the experimental datasets. However, the optimum fold was evaluated by testing the calibrated multipliers on the whole dataset instead of just the testing dataset from that fold. Figures 27 and 28 show the results of the calibration. It can be observed that the chains are well mixed, and the posterior distributions (both pair-wise and marginal distributions) are smooth for all four parameters, unlike the sharply peaked distributions observed in the previous study using the gradient boosted surrogates.

Table 9 shows the median values of the four Chisholm parameters for the five folds, and Table 10 shows the quantile and standard deviation values for the four Chisholm parameters for fold 2. With the optimum value for k_xkwlxChB fixed at 2.0, the optimum values for k_xkwlxChE and k_xkwlxChG are both close to their base values. k_xkwlxChA is slightly larger than the base value, indicating a slight increase on the impact of the slip ratio. Finally, an optimum k_xkwlxChF value close to the higher Reynolds number range in the Riso dataset lowers the pressure drop for high mass fluxes, with negligible impact for low mass fluxes/Reynolds numbers.

Table 9. Summary of the median (q50) values for all five folds

Fold	k_xkwlxChA (theta_1)	k_xkwlxChE (theta_2)	k_xkwlxChF (theta_3)	k_xkwlxChG (theta_4)
1	1.123	1.064	1.476e5	2.031
2	1.141	1.000	1.497e5	2.060
3	1.107	1.113	1.477e5	1.988
4	1.077	1.032	1.546e5	2.000
5	1.204	0.915	1.398e5	1.900

The impact of the calibrated (Fold-2) median multipliers can be seen in Fig. 29. The calibrated parameters (along with k_xkwlxChB = 2.0) roughly show a two-fold improvement in comparison to the base Chisholm model in terms of the RMSE. Three observations can be made regarding the parametric trends in 30. First, the impact of the mass flux parameter can be seen to give a fairly uniform trend in the pressure drop prediction with respect to mass flux. Second, the trend with system pressure also looks fairly uniform, with an over-prediction at low pressures. Third, there is a considerable over-prediction at low quality and an under-prediction at high quality. More work is required to improve the trend with quality, especially as the calibrated k_xkwlxChG value is close to the base value. Further investigation is also required to

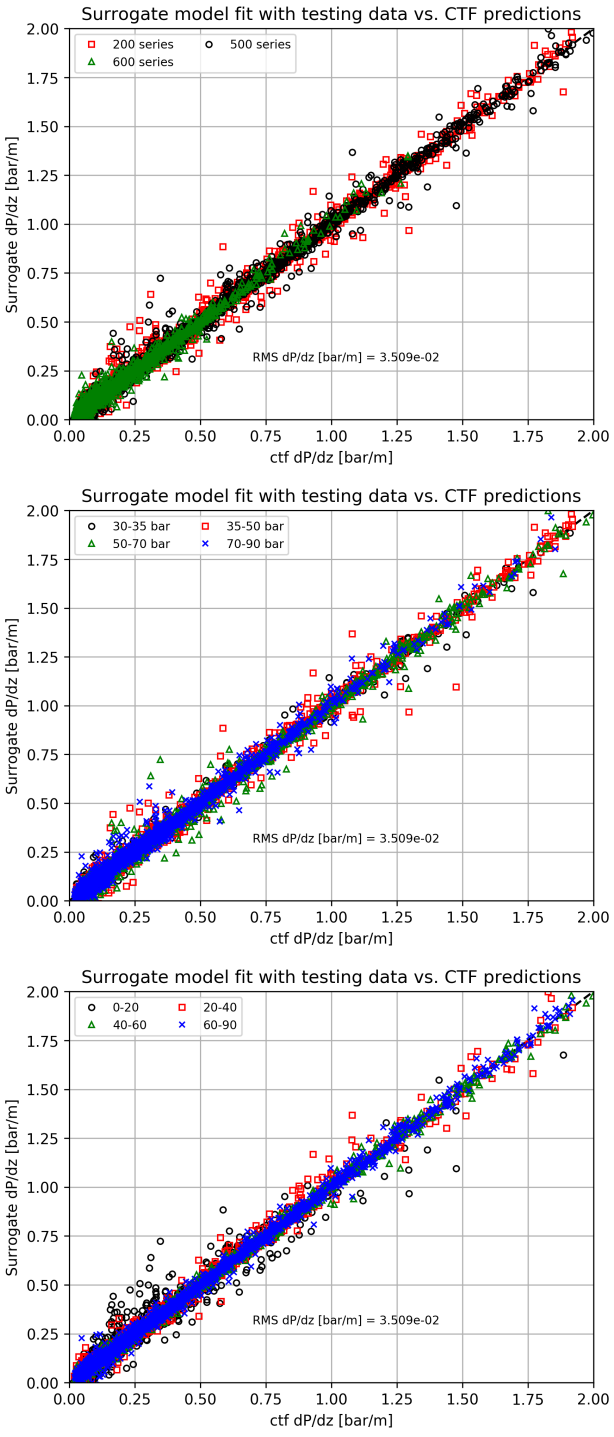

Figure 26. Risø surrogate model prediction for testing data colored by different: (a) series, (b) system pressure, and (c) inlet/exit quality.

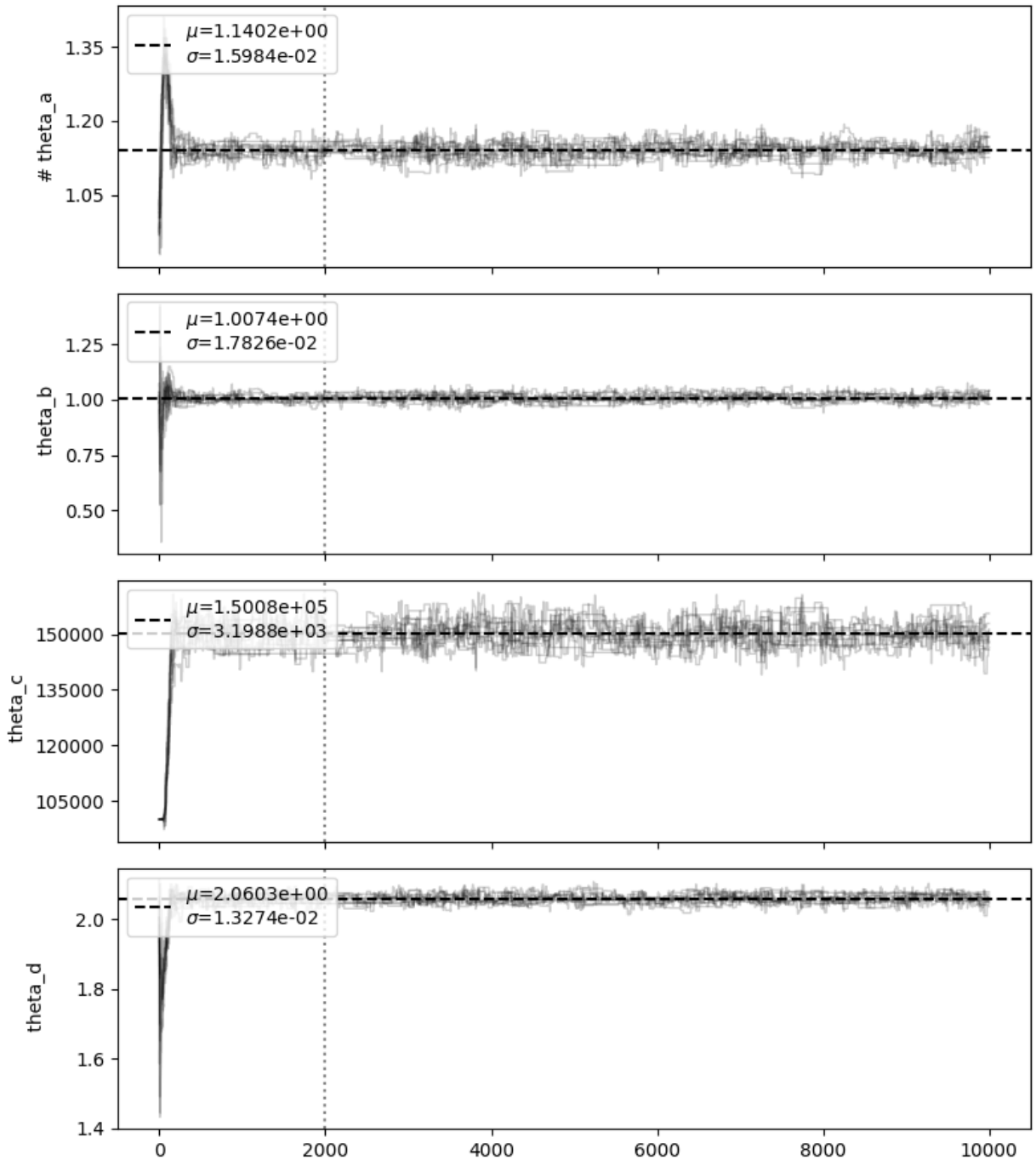

Figure 27. Change in the distribution of calibration multipliers for different chains as a function of sample size per chain.

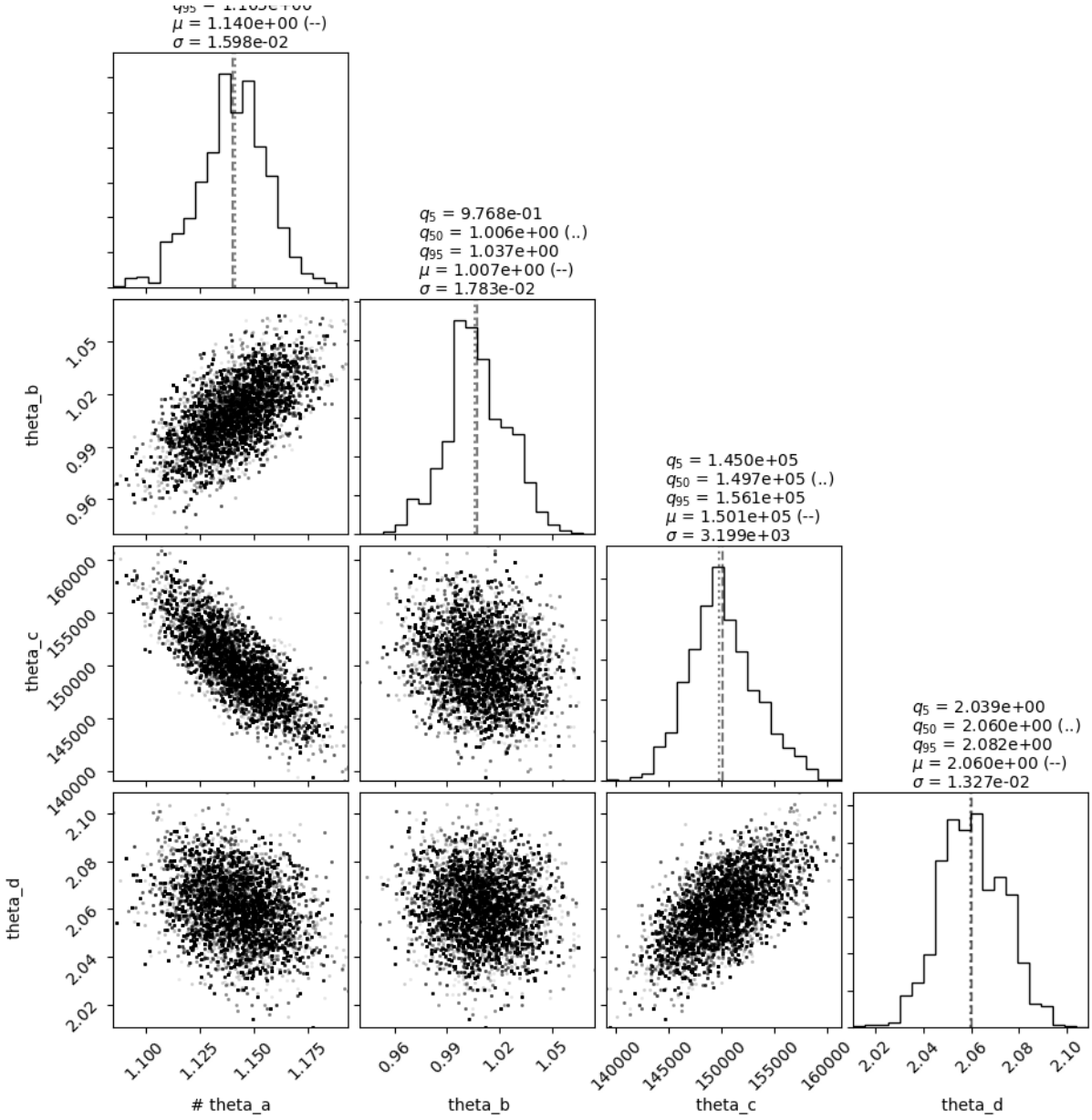

Figure 28. Final posterior distributions (pair-wise and marginal) of the calibration multipliers.

Table 10. Summary of calibration quantile and standard deviation values for Fold 2

Multiplier name	q5 value	q50 value	q95 value	$+/-1\sigma$
k_xkwlxChA (theta_1)	1.112	1.141	1.165	1.598e-2
k_xkwlxChE (theta_2)	0.977	1.006	1.037	1.783e-2
k_xkwlxChF (theta_3)	1.450e5	1.497e5	1.561e5	3.199e3
k_xkwlxChG (theta_4)	2.039	2.060	2.082	1.327e-2

develop better surrogates in general, especially with varying k_xkwlxChB. A comprehensive calibration of the type that was performed in the previous study should be performed by optimizing for both the interfacial drag model and the wall drag model simultaneously, even though the newer models are more strongly decoupled to each other than the base models.

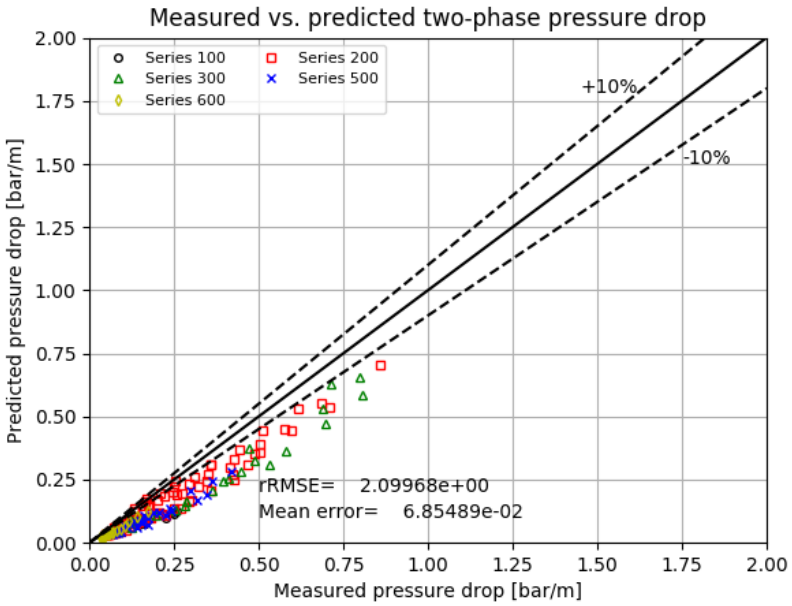

(a) Base Chisholm model

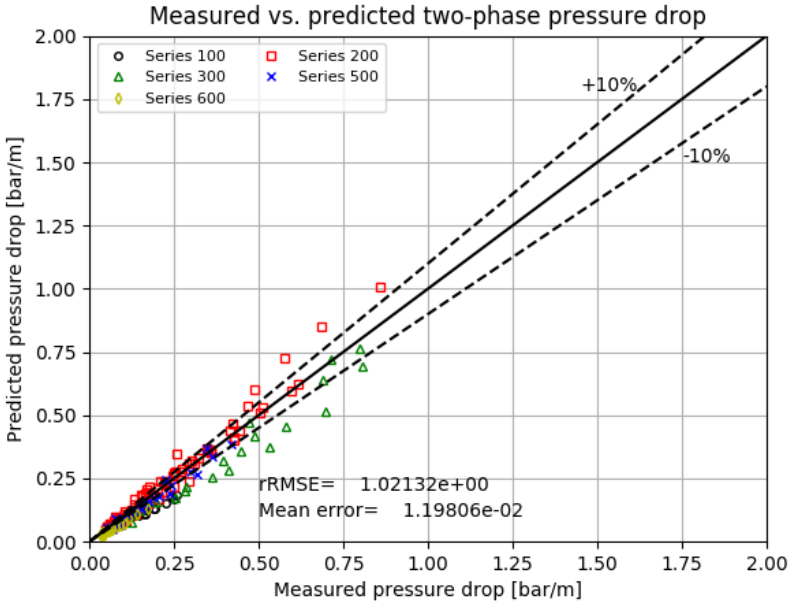

(b) Calibrated Chisholm model

Figure 29. Risø comparison of predicted and measured two-phase pressure drop with the base Chisholm and calibrated Chisholm models using the following closure models: drift-flux interfacial drag model, GE flow-regime, and Saha-Zuber subcooled boiling model (heated cases).

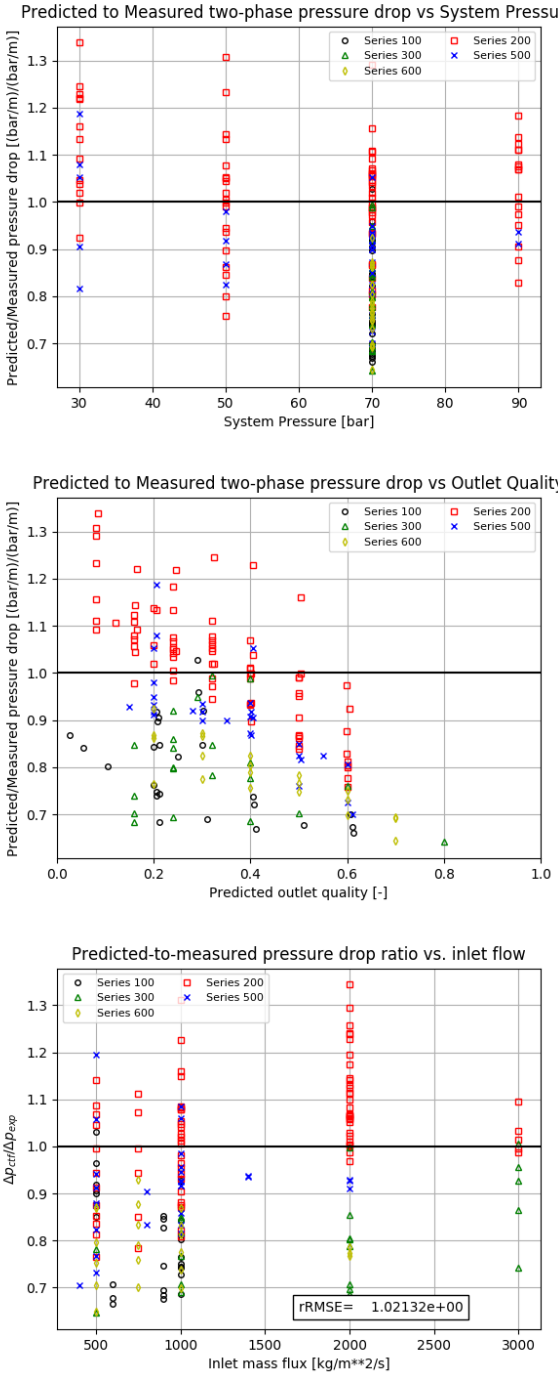

Figure 30. Risø measured-to-predicted two-phase pressure drop against (a) system pressure, (b) inlet/exit quality, and (c) inlet flow rate.

5. SUMMARY

The work performed as part of this milestone has led to improvements in BWR modeling accuracy through improvements to CTF closure models for two-phase pressure drop, wall heat transfer, implicit heat transfer, and the criteria for determination of the flow regime. Specifically, improvements and corrections were made to the wall heat transfer model that were originally implemented in Salko et al. [2020b], and corrections were made to the phase change model in CTF, which led to improvements in prediction of void over legacy models.

For the two-phase pressure drop, the Chisholm model was implemented for determination of the two-phase multiplier. The motivation for implementing this quality-based model was (1) to reduce the coupling between interfacial drag and wall drag, and (2) to test a new model for the Riso tests, which were previously over-predicted by the legacy Wallis model that was previously in CTF. Prediction of two-phase pressure drop is important for determination of the correct inlet flow distribution in BWR assemblies, which have physical barriers that prevent cross-flow in the core. The base Chisholm model led to an under-prediction of two-phase pressure drop that was similar in magnitude to the over-prediction of the Wallis model. To address this, an MCMC-based calibration was performed to recalibrate the Chisholm modeling parameters so that a better fit of the data was obtained.

Specifically related to the area of annular mist flow, a new flow regime map was implemented into the code to address the issue with over-prediction of the transition to annular flow. While the legacy CTF flow regime map can predict transition at unrealistically high voids of 90–95%, the new map can correctly predict the majority of the Riso tests in the annular mist flow regime. While the new closure models have generally improved void predictions in bubbly flow, they have also led to increased scatter of data in the annular mist flow regime in the BFBT bundle tests. This has prompted a review of the droplet interfacial drag models, which will now have a stronger effect since the flow regime is being correctly characterized. A new set of droplet interfacial drag models based on the drift-flux approach has been proposed and implemented into the code. The models are currently being tested and will be documented in a future report.

Finally, new experimental data were added to the two-phase validation matrix, which include additional annular geometry datasets from Riso that were previously unmodeled, as well as the FRIGG bundle void data. The FRIGG bundle data are different from the BFBT data because they include measurement of the axial void distribution, which is important for validating the onset of void and overall axial void distribution in the code.

While a great deal of work has been done in this report, there will be follow-on work to continue to improve CTF accuracy for BWRs. First, testing of the new droplet interfacial drag models must be completed, and one of the modeling options must be selected as the code default. Secondly, the calibration activities must be expanded to the interfacial drag models, as well as the heat transfer models. Third, during testing of the new models and perturbing modeling parameters as part of the sensitivity and calibration studies, it was found that the CTF numerical algorithm can be sensitive to changes, which can lead to instabilities and convergence difficulty. The authors believe this is due in-part to the explicitness of the coupling of the governing equations. A plan was presented in a previous milestone report (Salko et al. [2021]) for improving on the implicitness of the equations to remedy this issue. This plan will be implemented as part of future efforts.

6. REFERENCES

International Benchmark on Pressurized Water Reactor Sub-Channel and Bundle Tests. Volume II: Benchmark Results of Phase I—Void Distribution. Technical Report OECD/NEA/NSC/R(2015)4, Organisation for Economic Co-operation and Development Nuclear Energy Agency Nuclear Science Committee, 2016.

A. Abarca, M. Avramova, R. Salko, B. Hizoum, and M. Asgari. BWR Bypass Modeling in CTF. Technical Report M2EX-19OR04010118, North Carolina State University, 2021.

Mohamed Amine Bouhlel, John T. Hwang, Nathalie Bartoli, Remi Lafage, Joseph Morlier, and Joaquim R. R. A. Martins. A Python Surrogate Modeling Framework with Derivatives. *Advances in Engineering Software*, page 102662, 2019. ISSN 0965-9978. doi: https://doi.org/10.1016/j.advengsoft.2019.03.005.

D. Chisholm. Pressure Gradients Due to Friction during the Flow of Evaporating Two-Phase Mixtures in Smooth Tubes and Channels. *Int J Heat and Mass Transfer*, 16:347–358, 1973.

Daniel E Finkel. *Global Optimization with the DIRECT Algorithm*. North Carolina State University, 2005.

GE. *Licensing Topical Report TRACG MODEL DESCRIPTION*. Ge, 2008.

GEH. *GEH Licensing Topical Report NEDO-32176, Revision 4,TRACG Model Description*, 2008.

D. Gorenflo and D. Kenning. *VDI Heat Atlas*. VD-Verlag GmbH, Springer, Dusseldorf, 2nd edition, 1993.

W. Gurecky. Bayesian Inference for Python using Markov Chain Monte Carlo (BiPyMc). https://github.com/wgurecky/bipymc, 2018.

M. Ishii. One-Dimensional Drift-Flux Model and Constitutive Equations for Relative Motion between Phases in Various Two-Phase Flow Regimes. Technical Report ANL-77-47, Argonne National Laboratory, September 1977.

M. Ishii. Interfacial Transfer in Annular Dispersed Flow. Technical Report DE83 009571, Argonne National Laboratory, September 1982.

M. Ishii. Thermo-Fluid Dynamics of Two-Phase Flow. Technical Report ISBN 978-1-4419-7984-1, Argonne National Laboratory, 2011.

V. Kumar and R. Salko. Implementation of a New Wall Boiling Model in CTF. In *2020 ANS Virtual Winter Meeting*, 2020.

R. A. Lefebvre, B. R. Langley, P. Miller, M. Delchini, M. L. Baird, and J. P. Lefebvre. NEAMS Workbench Status and Capabilities. Technical Report ORNL/TM-2019/1314, Oak Ridge National Laboratory, 2019.

Takashi Hibiki Mamoru Ishii. Interfacial Transfer in Annular Dispersed Flow. Technical Report NUREG/CR-2885 ANL-82-44, School of Nuclear Engineering Purdue University West Lafayette, IN, USA, July July 1982.

Kacouiro Mishima and Mamouri Ishii. Flow Regime Transition Criteria for Upward Two-Phase Flow in Vertical Tubes. *International Journal of Heat and Mass Transfer Vol.27, No5, pp.723-737,1984*, 1987.

O. Nylund and R. Eklund. OF-64. Result of Void Measurement. Technical Report FRIGG-PM-69, ASEA-ATOM, 1970.

F. Pedregosa, G. Varoquaux, A. Gramfort, V. Michel, B. Thirion, O. Grisel, M. Blondel, P. Prettenhofer, R. Weiss, V. Dubourg, J. Vanderplas, A. Passos, D. Cournapeau, M. Brucher, M. Perrot, and E. Duchesnay. Scikit-learn: Machine learning in Python. *Journal of Machine Learning Research*, 12: 2825–2830, 2011.

Carl Edward Rasmussen and Christopher K. I. Williams. *Gaussian Processes for Machine Learning (Adaptive Computation and Machine Learning)*. The MIT Press, 2006. ISBN 026218253X.

S. Rouhani and E. Axelsson. Calculation of Void Volume Fraction in the Subcooled and Quality Boiling Regions. *International Journal of Heat and Mass Transfer*, 13(2):383–393, 1970.

R. Salko and V. Kumar. Assessment of CTF Needs for Modeling of Boiling Water Reactors. Technical Report ORNL/TM-2020-3, Oak Ridge National Laboratory, 2020.

R. Salko, A. Wysocki, M. Avramova, A. Toptan, N. Porter, T. Blyth, C. Dances, A. Gomez, C. Jernigan, and J. Kelly. *CTF Theory Manual*. North Carolina State University, 2017a.

R. Salko, A. Wysocki, J. Gehin, M. Avramova, A. Toptan, N. Porter, T. Blyth, C. Dances, J. Magedanz, M. Gergar, C. Gosdin, C. Jernigan, J. Kelly, and S. Palmtag. *CTF Validation and Verification*. North Carolina State University, 2017b.

R. Salko, B. Hizoum, B. Collins, and M. Asgari. Improvements to CTF for Modeling of Boiling Water Reactor Geometry and Operating Conditions. Technical Report ORNL/TM-2020/1746, Oak Ridge National Laboratory, 2020a.

R. Salko, V. Kumar, and B. Hizoum. Improvements to CTF Closure Models for Modeling of Two-Phase Flow. Technical Report ORNL/TM-2020/3, Oak Ridge National Laboratory, 2020b.

R. Salko, B. Hizoum, A. Graham, B. Collins, and M. Asgari. Summary of CTF Modeling and Numerical Improvements for Boiling Water Reactor Simulation. Technical Report ORNL/TM-2021/2004, Oak Ridge National Laboratory, 2021.

Jasper A Vrugt, James M Hyman, Bruce A Robinson, Dave Higdon, Cajo J F Ter Braak, and Cees G H Diks. Accelerating Markov Chain Monte Carlo Simulation by Differential Evolution with Self-Adaptive Randomized Subspace Sampling. *International Journal of Nonlinear Sciences and Numerical Simulation*, 10(3), 1 2008.

G.B. Wallis. *One-Dimensional Two-Phase Flow*. McGraw-Hill, 1969.

Jorgen Wurtz. An Experimental and Theoretical Investigation of Annular Steam-Water Flow in Tubes and Annuli at 30 to 90 bar. Technical Report Riso Report No. 372, Riso National Laboratory, Copenhagen, Denmark, 4 1978.

A. Wysocki and R. Salko. Validation of CTF Droplet Entrainment and Annular/Mist Closure Models Using Riso Steam/Water Experiments. Technical Report CASL-U-2016-1080-000, Consortium for Advanced Simulation of Light Water Reactors, 2016.

Xingang Zhao, Aaron J. Wysocki, Koroush Shirvan, and Robert K. Salko. Assessment of the Subchannel Code CTF for Single- and Two-Phase Flows. *Nuclear Technology*, 205(1–2):338–351, 2019.